

PAPER • OPEN ACCESS

The poloidal distribution of electrostatic zonal flow drive in strongly shaped tokamaks

To cite this article: T M Schuett et al 2025 Plasma Phys. Control. Fusion 67 115022

View the article online for updates and enhancements.

You may also like

- The dynamic age of Centaurus A Jean A Eilek
- Mapping 1+1-dimensional black hole thermodynamics to finite volume effects
 Jean Alexandre, Drew Backhouse, Eleni-Alexandra Kontou et al.
- <u>The 2024 acoustic metamaterials roadmap</u> G J Chaplain, F Langfeldt, V Romero-García et al.

Plasma Phys. Control. Fusion 67 (2025) 115022 (18pp)

https://doi.org/10.1088/1361-6587/ae175c

The poloidal distribution of electrostatic zonal flow drive in strongly shaped tokamaks

T M Schuett* , I Cziegler and D Dickinson

York Plasma Institute, School of Physics, Engineering and Technology, University of York, Heslington YO10 5DD, United Kingdom

E-mail: tobias.schuett@york.ac.uk

Received 6 September 2025, revised 14 October 2025 Accepted for publication 24 October 2025 Published 14 November 2025



Abstract

Knowledge of the poloidal distribution of zonal flow (ZF) drive has been a missing yet crucial component of both our understanding of turbulence–flow interactions and the validation of gyrokinetic codes. We present the first analysis of the distribution of electrostatic ZF drive due to Reynolds stress. Using gyrokinetic flux-tube simulations we examine the effect of strong axisymmetric shaping, including elongation, triangularity, and aspect ratio, as well as up–down asymmetric equilibria. With increased shaping, the ZF drive develops local maxima near those of poloidal curvature, with a tendency to shift towards the so-called bad curvature side. Thus, depending on the shaping, the nonlinear ZF drive may not peak at the outboard midplane where the turbulent fluctuations are the strongest and where turbulence diagnostics are usually located. Our results therefore suggest that a shaping correction must be taken into account when extrapolating from a poloidally localized measurement to the total electrostatic ZF drive on a flux-surface.

Keywords: ITG, zonal flows, Reynolds stress, nonlinear coupling, gyrokinetics

1. Introduction

Turbulent transport driven by the free energy of the equilibrium temperature and density gradients is responsible for the majority of the radial heat and particle transport in tokamaks and optimized stellarators [1, 2]. Fortunately, turbulence has the ability to self-organize into meso-scale flows. These flows are directed in the binormal direction, i.e. the flow direction is perpendicular to both the field line and the flux surface normal vector. While they are poloidally and toroidally symmetric, they cover a narrow radial zone and are thus termed zonal

Original Content from this work may be used under the terms of the Creative Commons Attribution 4.0 licence. Any further distribution of this work must maintain attribution to the author(s) and the title of the work, journal citation and DOI.

flows (ZFs). ZFs are linearly stable and therefore unable to feed off the free energy supplied by the gradients. They do not contribute to radial transport, but lessen the impact of the radially elongated and therefore most detrimental turbulent eddies by shearing them apart [3, 4]. In addition to this modification of the typical eddy length scales, ZFs also modify the turbulent fluctuation power by taking energy directly out of them via nonlinear coupling. It is the strength of this nonlinear coupling which determines the drive of ZFs in the system.

Since ZFs are poloidally symmetric and the turbulent fluctuations generally peak at the outboard midplane, this naturally raises the question about the poloidal distribution of their nonlinear interaction. While it is the mean $\mathbf{E} \times \mathbf{B}$ shearing which sustains confinement states [5] such as the high confinement mode (H-mode) [6], ZFs can trigger a transition from the low confinement mode (L-mode) into the H-mode by transiently increasing the $\mathbf{E} \times \mathbf{B}$ shear, after receiving energy nonlinearly from turbulent modes. This interaction takes place whenever a radial gradient of the turbulent Reynolds stress is present [7].

^{*} Author to whom any correspondence should be addressed.

It has been shown experimentally that this drive increases with heating power [8], and that the onset of confinement transitions such as the L–H transition is directly linked to a critical drive of ZFs [9–11]. The interpretation of such measurements which are often taken at the outboard midplane would greatly benefit from a theoretical prediction of the ZF drive envelope for varying macroscopic equilibrium parameters, especially due to limited diagnostic coverage. If the ZF drive at the outboard midplane varies significantly with plasma shaping such a theoretical prediction renders it possible to compare and interpret localized experimental results from discharges with different plasma shaping.

A prior analysis for the Cyclone base case (CBC) [12], a widely used tokamak benchmark equilibrium with circular plasma shaping and aspect ratio A = 2.72, showed that the poloidal distribution of the coupling is correlated with the turbulent fluctuation level but not strictly proportional to it [13]. However, all modern tokamaks and reactor studies rely on strong plasma shaping due to the benefits for MHD stability [14] as well as turbulent transport [15–17]. It was recently shown that the linear damping of ZFs varies between positive and negative triangularity (NT) [18] and that the poloidal envelope of the mean $\mathbf{E} \times \mathbf{B}$ shearing rate changes with plasma shaping [19]. These strong shaping effects in both macroscopic and linear microscopic turbulence dynamics further motivate a closer look at the nonlinear microscopic turbulence dynamics and the associated nonlinear coupling responsible for the drive of ZFs. This nonlinear interaction between turbulent modes and zonal modes is described by three-wave coupling and can be quantified with the help of bispectral methods and the closely related energy transfer functions [20, 21]. A kinetic formulation of such energy transfer functions has also been used for the analysis of the multi-scale coupling between ion and electron scale turbulence [22, 23]. In previous work the qualitative dynamics of the fluid internal energy transfer has been successfully validated at the outboard midplane between experiments and gyrokinetic simulations [24]. Here we use the gyrokinetic code GS2 [25, 26] to evaluate the fluid kinetic energy transfer along a field-line-following magnetic flux tube. In an axisymmetric system, which we are considering in this paper, this directly yields information about the full poloidal distribution.

This paper is structured as follows. In section 2 we introduce the shaping formalism, give a brief introduction to gyrokinetics, and introduce the nonlinear transfer theory. Section 3 discusses the individual and finally combined effects of elongation, triangularity, and aspect ratio as well as updown asymmetry on the poloidal distribution of the ZF drive. Transfer proxy functions are proposed and evaluated. Finally, we conclude in section 4.

2. Methods

2.1. Equilibrium model

We aim to treat realistic plasma shaping, thereby expanding on the CBC, the most used tokamak benchmark equilibrium, which has circular nested flux surfaces. As in the CBC we neglect collisions as well as equilibrium flow and flow shear. The shaped flux surfaces are specified through the original Miller parametrization of axisymmetric MHD equilibria [27],

$$R(\vartheta) = R_0 + r\cos[\vartheta + \delta\sin\vartheta],\tag{1}$$

$$Z(\vartheta) = \kappa r \sin \vartheta. \tag{2}$$

Here R_0 is the major radius, r the minor radius of the simulated flux surface, δ the triangularity¹, and κ the elongation. In total the Miller equilibria are specified through nine independent parameters which are summarized in table 1.

The flux surfaces are specified in terms of the poloidal Miller angle ϑ which is generally different to the geometric arctangent angle

$$\theta(\vartheta) = \arctan\left(\frac{Z(\vartheta)}{R(\vartheta) - R_0}\right) \tag{3}$$

which will be used throughout this paper. We also consider up—down asymmetric equilibria obtained by tilting the elongation or triangularity in the poloidal plane. These cases require a generalized Miller parameterization which was previously derived and implemented in GS2 [28, 29].

2.2. Turbulence model

With validation in mind we choose the turbulence model to be the one that is most complete while computationally feasible for parameter scans: nonlinear local gyrokinetics. To this end we use the open-source code GS2 [25, 26] which solves the nonlinear gyrokinetic equation for both electrostatic and electromagnetic turbulence in a flux tube.

Here we are interested in the electrostatic limit with no equilibrium flow and flow shear. The nonlinear local gyrokinetic equation then reads [30]

$$\frac{\partial g_{s}}{\partial t} + (v_{\parallel} \mathbf{b} + \mathbf{V}_{Ds}) \cdot \nabla_{\mathbf{R}} h_{s} + \mathcal{N}_{s} + \frac{\partial F_{0s}}{\partial \psi} \langle \mathbf{V}_{E \times B} \rangle_{\mathbf{R}} \cdot \nabla_{\mathbf{R}} \psi = 0.$$
(4)

Here s is the species label and g_s is the gyro-average of δf_s , the fluctuating part of the full distribution function $f_s = F_{0s} + \delta f_s$. Here F_{0s} is the zeroth-order contribution and is Maxwellian,

$$F_{0s}(\psi, \varepsilon_s) = n_{0s}(\psi) \left(\frac{m_s}{2\pi T_{0s}(\psi)}\right)^{3/2} \exp\left(-\frac{\varepsilon_s}{T_{0s}(\psi)}\right), (5)$$

where ψ is the toroidal magnetic flux, n_{0s} is the equilibrium density, T_{0s} the equilibrium temperature, and $\varepsilon_s = m_s |\mathbf{v}|^2/2$ the particle energy with particle velocity \mathbf{v} . The fluctuating part of the distribution function δf_s can be split up according to $\delta f_s = h_s - (Z_s e \delta \phi / T_{0s}) F_{0s}$, where h_s is now independent of the gyro-angle coordinate, and $\delta \phi$ is the leading order fluctuation of the electrostatic potential. Thus $g_s = \langle \delta f_s \rangle_{\mathbf{R}} =$

¹ This definition of triangularity is related to the original definition in Miller's paper through $\delta \equiv \arcsin \delta_M$.

Name	Symbol	Variable Name	CBC Value	Other values used
minor radius and reference length	а	N/A	0.625	<u> </u>
norm. minor radius of flux surface	$\rho = r/a$	rhoc	0.8	_
norm. major radius of equilibrium	R_0/a	rmaj	2.72	2.0, 1.4
†inverse aspect ratio of equilibrium	a/R_0	eps	0.37	0.5, 0.71
†elongation of flux surface	κ	akappa	1.0	1.5, 2.0
†radial variation of elongation	$\partial_r \kappa$	akappri	0.0	$1-\kappa$
†triangularity of flux surface	$\delta \equiv \arcsin \delta_M$	tri	0.0	$\pm 0.25, \pm 0.5, \pm 0.75$
†radial variation of triangularity	$\partial_r \delta$	tripri	0.0	$\delta/\sqrt{1-\delta^2}$
†safety factor	q	qinp	1.4	4.0
†global magnetic shear	\hat{s}	shat	0.78	_
†re-scaled pressure gradient	$lpha_{ ext{MHD}}$	alpha_input	0.0	_
†radial variation of major radius	$\partial_r R_0$	shift	0.0	

Table 1. The nine Miller parameters (marked with †) and other quantities used to define them. The columns represent the variable names in GS2, their value for the Cyclone base case (CBC), and other values used in this work.

 $h_s - (Z_s e \langle \delta \phi \rangle_{\mathbf{R}} / T_{0s}) F_{0s}$, where $\langle . \rangle_{\mathbf{R}}$ represents a gyro-average at constant guiding-center position \mathbf{R} , which is related to the particle position \mathbf{r} via $\mathbf{r} = \mathbf{R} + \boldsymbol{\rho}$ where $\boldsymbol{\rho}$ is the gyro-radius vector.

The other terms in the gyrokinetic equation (4) are the parallel velocity $v_{\parallel} = \mathbf{v} \cdot \mathbf{b}$, the guiding-center drift $\mathbf{V}_{Ds} = (2\Omega_s)^{-1}\mathbf{b} \times [2\nu_{\parallel}^2\mathbf{b} \cdot \nabla \mathbf{b} + \nu_{\perp}^2 \nabla \ln \mathbf{B}]$ with $\nu_{\perp} = |\mathbf{v}| - \nu_{\parallel}$ and the unit vector along the field $\mathbf{b} = \mathbf{B}/B$, and the gyrokinetic nonlinearity $\mathcal{N}_s = \langle \mathbf{V}_{E\times B} \rangle_{\mathbf{R}} \cdot \nabla_{\mathbf{R}} h_s$ with $\mathbf{V}_{E\times B} = -\nabla(\delta\phi) \times \mathbf{B}/B^2$. Here $\nabla_{\mathbf{R}}$ denotes the gradient operator at fixed \mathbf{R} .

In the electrostatic limit the system is closed by Poisson's equation which reduces to quasi-neutrality $\sum_s Z_s \delta n_s = 0$. In this paper we only treat ions gyrokinetically and use an adiabatic electron model $\delta n_{\rm e} = e n_{0\rm e} (\delta \phi - \overline{\delta \phi})/T_{0\rm e}$, where the overline denotes a field-line-average and we take $n_{0\rm e} = n_{0\rm i}$ and $T_{0\rm e} = T_{0\rm i}$. In this case quasi-neutrality reduces to

$$\int d\mathbf{v} \langle g_i \rangle_{\mathbf{r}} = \frac{e n_{\rm e}}{Z_i T_{\rm e}} \left(\delta \phi - \overline{\delta \phi} \right), \tag{6}$$

where $\langle . \rangle_{\mathbf{r}}$ denotes the (dual) gyro-average at constant \mathbf{r} [31]. The flux tube is centered around a chosen field line for one polaidal turn. The perpendicular extent of the simple

one poloidal turn. The perpendicular extent of the simulation domain is chosen small enough that geometric quantities and equilibrium gradients can be assumed constant throughout, but large enough that turbulence quantities are statistically identical at the boundaries and periodic boundary conditions can be used. As a result fluctuating quantities such as the electrostatic potential are evolved in Fourier space and are expressed as

$$\delta\phi(x, y, z, t) = \sum_{\mathbf{k}} \delta\phi_{\mathbf{k}}(z, t) \exp[i(k_x x + k_y y)], \qquad (7)$$

where $\mathbf{k} = k_x \nabla x + k_y \nabla y$ is the perpendicular wave-vector, and z is the parallel coordinate which we choose to be equal to the poloidal angle, $z = \theta$, though other definitions are possible. In the above x and y are field-aligned radial and binormal coordinates that are proportional to ψ and the field line label α ,

$$x = \frac{q_0}{B_0 r_0} (\psi - \psi_0)$$
 and $y = -\frac{r_0}{q_0} (\alpha - \alpha_0)$, (8)

but now have units of length [32]. Here α_0 and ψ_0 are the values at the center of the flux tube, where the safety factor takes on the value $q_0 = q(\psi_0)$ and the minor radius is $r_0 = r(\psi_0)$; B_0 is the on-axis magnetic field strength. The field line label alpha is defined as $\alpha = \zeta - q\theta$ where θ and ζ are the poloidal and toroidal straight-field-line angles. Due to the finite magnetic shear so-called twist and shift boundary conditions are used in the parallel direction [32].

The drive for ITG turbulence is set by the fixed equilibrium ion temperature and density gradients, specified through their normalized scale lengths

$$\frac{a}{L_n} \equiv -\frac{a}{n} \frac{\mathrm{d}n}{\mathrm{d}r} \quad \text{and} \quad \frac{a}{L_T} \equiv -\frac{a}{T} \frac{\mathrm{d}T}{\mathrm{d}r}.$$
 (9)

Here r is the half diameter at the outboard midplane, following the convention in tokamak gyrokinetics. For the CBC the values are $a/L_n = 0.81$ and $a/L_T = 2.49$. Non-circular flux surface shaping is known to yield reduced heat fluxes [15], so to prevent our shaped cases from becoming marginal we increase the temperature gradient drive to $a/L_T = 6.0$ (or even higher where explicitly stated).

An extensive introduction to gyrokinetics as implemented in GS2 is given in [31] and the numerical details are well described in [33].

2.3. Obtaining the Reynolds stress

The Reynold stress drive of ZFs is contained within the convective derivative of the momentum equation [7]. We therefore analyze the ZF drive in the fluid picture, using the fluctuating electrostatic potential of the gyrokinetic simulations. This is motivated by comparison with experiment, similar to the approach taken in [24].

To obtain an expression for the ZF drive we follow the method from [20]. We start by writing the momentum equation as

$$\frac{\partial \mathbf{V}}{\partial t} = -\mathbf{V} \cdot \nabla \mathbf{V} + \mathcal{L},\tag{10}$$

where we have combined the pressure gradient force, the Lorentz force, the inter-species friction force, and the viscosity tensor into the general linear operator \mathcal{L} . In the electrostatic case these terms do not contain a nonlinearity of fluctuation quantities, and are therefore not of importance for the *nonlinear* drive of ZFs.

To make progress in analyzing the nonlinearity a Fourier decomposition is required. In line with the gyrokinetic ordering we assume parallel wavelengths to be much longer than perpendicular ones, $k_{\parallel} \sim \epsilon k_{\perp}$, and effectively reduce the system to the perpendicular plane

$$\frac{\partial \mathbf{V_k}}{\partial t} = -\sum_{\mathbf{k_1}} (\mathbf{V_{k-k_1}} \cdot i\mathbf{k_1}) \mathbf{V_{k_1}} + \mathcal{L}_{\mathbf{k}}.$$
 (11)

The nonlinearity now appears as a convolution which highlights the underlying three-wave coupling of \mathbf{k} , \mathbf{k}_1 and \mathbf{k}_2 with the selection rule $\mathbf{k} - \mathbf{k}_1 = \mathbf{k}_2$. Note that compared to [20] we express the coupling to be in wavenumber-space rather than frequency-space. While experimental measurements offer high temporal resolution but limited spatial resolution, the opposite tends to be the case in turbulence simulations, making this the natural choice.

After multiplying equation (11) by V_k^* , then adding the resulting expression to its conjugate, and finally taking an ensemble average, one obtains a conservation equation for the fluid kinetic energy

$$\left\langle \frac{1}{2} \frac{\partial |\mathbf{V}_{\mathbf{k}}|^{2}}{\partial t} \right\rangle = -\left\langle \operatorname{Re} \left\{ \sum_{\mathbf{k}_{1}} \mathbf{V}_{\mathbf{k}}^{*} \cdot \left[(\mathbf{V}_{\mathbf{k} - \mathbf{k}_{1}} \cdot i\mathbf{k}_{1}) \, \mathbf{V}_{\mathbf{k}_{1}} \right] \right\} \right\rangle + \left\langle \operatorname{Re} \left\{ \mathbf{V}_{\mathbf{k}}^{*} \mathcal{L}_{\mathbf{k}} \right\} \right\rangle. \tag{12}$$

Here $\langle . \rangle$ denotes the ensemble average realized in the form of temporal averaging (over the saturated period of the simulations) due to ergodicity [34].

We make further progress by approximating the fluid velocity by $\mathbf{E} \times \mathbf{B}$ motion, $\mathbf{V} = B^{-1}\mathbf{b} \times \nabla \delta \phi$ or $\mathbf{V_k} = B^{-1}\mathbf{b} \times i\mathbf{k}\delta\phi_{\mathbf{k}}$. The final expression then reads

$$\left\langle \frac{1}{2} \frac{\partial |\mathbf{V}_{\mathbf{k}}|^2}{\partial t} \right\rangle = \sum_{\mathbf{k}_1} \mathcal{T}_{\nu}(\mathbf{k}, \mathbf{k}_1, \theta) + \left\langle \operatorname{Re} \left\{ \mathbf{V}_{\mathbf{k}}^* \mathcal{L}_{\mathbf{k}} \right\} \right\rangle$$
(13)

Here the first term on the right-hand side is the kinetic energy transfer function.

$$\mathcal{T}_{\nu}(\mathbf{k}, \mathbf{k}_{1}, \theta) = B^{-3} \langle \operatorname{Re}\{(\mathbf{b} \times \mathbf{k} \delta \phi_{\mathbf{k}}^{*}) \cdot [(\mathbf{b} \times \mathbf{k} \delta \phi_{\mathbf{k} - \mathbf{k}_{1}}) \cdot \mathbf{k}_{1}(\mathbf{b} \times \mathbf{k}_{1} \delta \phi_{\mathbf{k}_{1}})]\} \rangle$$

$$= W(\mathbf{k}, \mathbf{k}_{1}) \operatorname{Re}\langle \delta \phi_{\mathbf{k}}^{*} \delta \phi_{\mathbf{k} - \mathbf{k}_{1}} \delta \phi_{\mathbf{k}_{1}} \rangle. \tag{14}$$

The weighting factor $W(\mathbf{k}, \mathbf{k}_1) = B^{-3}[\mathbf{b} \times \mathbf{k} \cdot \mathbf{k}_1](\mathbf{b} \times \mathbf{k}) \cdot (\mathbf{b} \times \mathbf{k}_1)$ ensures the correct wavenumber weighting to describe the transfer of kinetic energy. \mathcal{T}_{ν} thus resolves the nonlinear transfer of (fluid) kinetic energy from the source mode \mathbf{k}_1 to the target mode \mathbf{k} through the corresponding mediator mode \mathbf{k}_2 at a given point θ along the flux tube. Compared to the more well-known bicoherence, this transfer function does not only indicate the magnitude of the coupling but also its direction. Thus, positive (negative) values of \mathcal{T}_{ν} correspond to a gain (loss) of energy in mode \mathbf{k} through the coupling with

 \mathbf{k}_1 [10, 20]. For the specific analysis in this paper we define the total drive of ZFs as

$$\mathcal{T}_{\nu}^{\text{ZF}}(\theta) \equiv \sum_{k_{x}, k_{1x}, k_{1y}} \mathcal{T}_{\nu}(k_{x}, k_{y} = 0, k_{1x}, k_{1y}, \theta).$$
 (15)

The computation of \mathcal{T}_v was implemented as a Python post-processing tool for GS2 as part of prior work by Biggs–Fox [13] and has now been implemented as a diagnostic to GS2, allowing for memory efficient MPI parallelized computation at runtime. The diagnostic has been made available in the recently released GS2 version 8.2.0 [25].

3. Results

In the following we analyze the nonlinear transfer for isolated variations in elongation, triangularity and aspect ratio, bridging the gap from the circular shaping of the CBC to the typical highly shaped and low aspect ratio equilibria of spherical tokamaks. In a final step we combine all three shaping parameters to obtain a typical spherical tokamak equilibrium.

3.1. Elongation

We first focus on the linear growth rate dependence on the temperature gradient and elongation to motivate the chosen range for the nonlinear analysis. Linear initial-value calculations were performed with GS2 for varying temperature gradient and elongation. The maximum growth rate and its corresponding wavenumber for each combination are shown on the left in figure 1.²

The results on the left in figure 1 show the known trend that ITG turbulence is stabilized by both a lower temperature gradient and higher elongation [15–17]. Motivated by these results we choose $a/L_T=6.0$ to perform a three-point-scan in elongation for the nonlinear study. We consider cases with $\kappa \in \{1.0, 1.5, 2.0\}$ and correspondingly vary its radial derivative with $\partial_r \kappa = \kappa - 1$ for a reasonable shaping penetration estimate [27]. Although the actual radial flux-surface shaping penetration has a non-trivial dependency on the poloidal variation of the poloidal magnetic field and the toroidal current profile [35], the estimate used should be sufficient for the local approach taken here. The right plot in figure 1 shows the maximum linear growth rate as well as the total nonlinear turbulent activity across the $a/L_T=6.0$ slice. Here we define the total nonlinear turbulent activity as the mean fluctuations amplitude

 $^{^2}$ Convergence was tested at the four most extreme cases, $[a/L_T \in \{4.0,7.0\}] \times [\kappa \in \{1.0,2.0\}]$, upon doubling the parallel grid and number of trapped particles (ntheta), the energy grid (negrid), the number of passing particles (ngauss), the simulation time (max_sim_time), as well as halving the time step (delt) and extending the parallel domain. For further details see appendix A.

³ The strong dependence on elongation results since temperature gradients are specified at the midplane in standard tokamak gyrokinetic studies [16, 17].

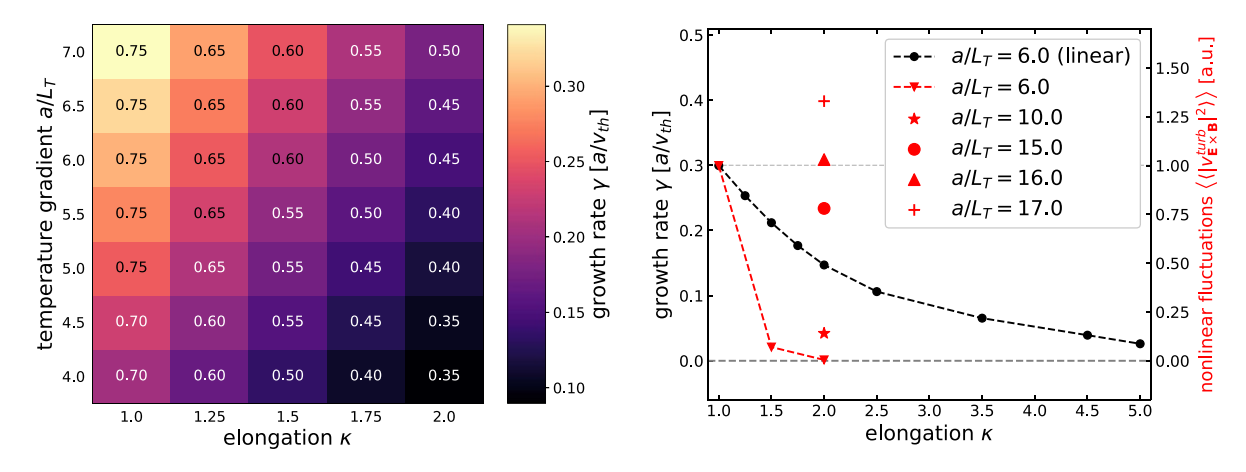


Figure 1. Linear and nonlinear response to varying elongation and temperature gradient. Left: The maximum linear growth rate as a function of elongation and temperature gradient with the value of the normalized binormal wavenumber, $k_y \rho_r$, corresponding to the maximum growth rate overlaid. Right: A slice through the left figure along $a/L_T = 6.0$. Results from nonlinear simulations with increased temperature gradient are included for $\kappa = 2.0$, showing that ($\kappa = 2.0$; $a/L_T = 16.0$) approximately matches the total turbulent fluctuation energy of ($\kappa = 1.0$; $a/L_T = 6.0$). The linear growth rate is also shown to highlight the Dimits shift [12].

of the turbulent (non-zonal) $\mathbf{E} \times \mathbf{B}$ velocity,

$$\left\langle \left\langle \left| \delta v_{\mathbf{E} \times \mathbf{B}}^{\text{turb}} \right|^{2} \right\rangle \right\rangle = \frac{1}{B^{2}} \sum_{k_{x}, k_{y} \neq 0} \left(k_{x}^{2} + k_{y}^{2} \right) \left\langle \left\langle \left| \delta \phi \left(\mathbf{k}, \theta, t \right) \right|^{2} \right\rangle \right\rangle.$$
(16)

 $\langle \langle . \rangle \rangle$ denotes temporal averaging over the saturated period of the simulations as well as poloidal averaging. A clear Dimits shift [12] is observed on the right in figure 1. Prior results hinted at the fact that \mathcal{T}_{ν}^{ZF} may also depend on how marginal the turbulence is [13], i.e. where it is located within the Dimits regime. For this reason we performed additional simulations with increased temperature gradient for $\kappa=2.0$, with the goal of matching the turbulent activity to the modified CBC case, and thus to isolate the effect of elongation from that of the proximity to marginality. The right plot in figure 1 shows that the turbulent fluctuation level at $(\kappa=2.0; a/L_T=16.0)$ approximately matches those at $(\kappa=1.0; a/L_T=6.0)$.

We evaluate $\mathcal{T}_{\nu}^{\mathrm{ZF}}(\theta)$ from equation (15) over the saturated period of the simulations. The resulting poloidal distributions are shown in figure 2, and mapped onto the analyzed flux surface $\rho = 0.8$ in figure 3. As the cross-section becomes elongated, the global maximum of ZF drive at the outboard midplane splits into two local maxima which are located near the top and bottom of the equilibria. However, we also note that they are shifted slightly outwards towards the region of so-called bad curvature, i.e. towards the outboard midplane where the turbulence is usually driven most strongly. The discrepancy between the maximum drive and the drive at the outboard midplane grows as elongation is increased.

In figure 4 we plot two measures of the turbulent activity against the poloidal angle. The left plot shows the poloidal distribution of the (unweighted) potential fluctuation energy, while the right plot shows the distribution of the

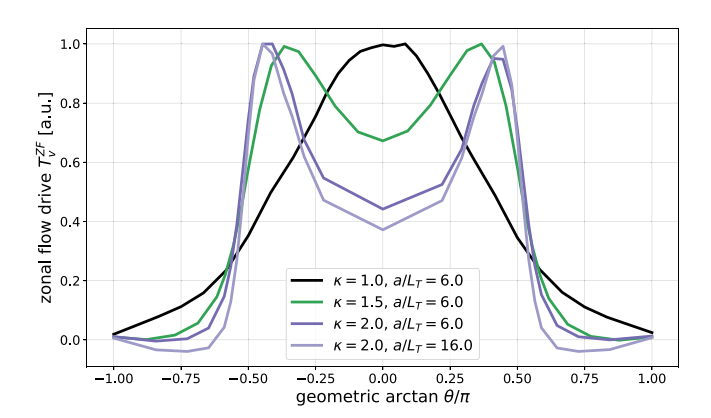


Figure 2. The poloidal distributions of the ZF drive with varying elongation and fixed gradient (solid) and the highly elongated case with matched fluctuation level (shaded purple).

 $\mathbf{E} \times \mathbf{B}$ fluctuation energy. Since the total fluctuation energy was established in figure 1 we now show the normalized distributions to highlight their poloidal structure. We note that for $\kappa = 2.0$ with $a/L_T = 6.0$ the poloidal structure of the $\mathbf{E} \times \mathbf{B}$ fluctuations resembles that of $\mathcal{T}_{\nu}^{\mathrm{ZF}}$ from figures 2 and 3. However, as the temperature gradient is increased, this similarity disappears and returns to a more ballooning-like structure, whereas the structure of the nonlinear ZF drive keeps its poloidal shape throughout the Dimits regime as shown in figure 2. The same effect is also observed for the electrostatic potential fluctuations in figure 4, albeit less pronounced.

3.2. Triangularity

Most axisymmetric plasma shaping used today features both significant elongation and triangularity. Whereas traditionally triangularity has mostly been positive, i.e. with the nose of the

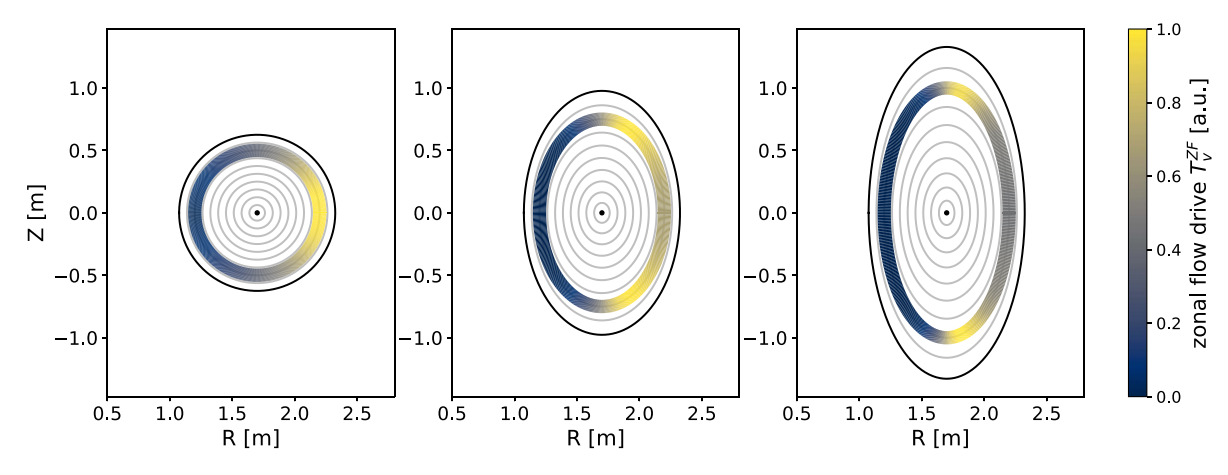


Figure 3. The poloidal distributions of the ZF drive mapped onto the poloidal cross-section for fixed temperature gradient $a/L_T = 6.0$. Each case has been normalized independently, so absolute values of \mathcal{T}_v^{ZF} should not be compared between different equilibria. The radial width of the colored region is for illustrative purposes only. Left: Cyclone base case (CBC). Center: Elongation $\kappa = 1.5$. Right: Elongation $\kappa = 2.0$.

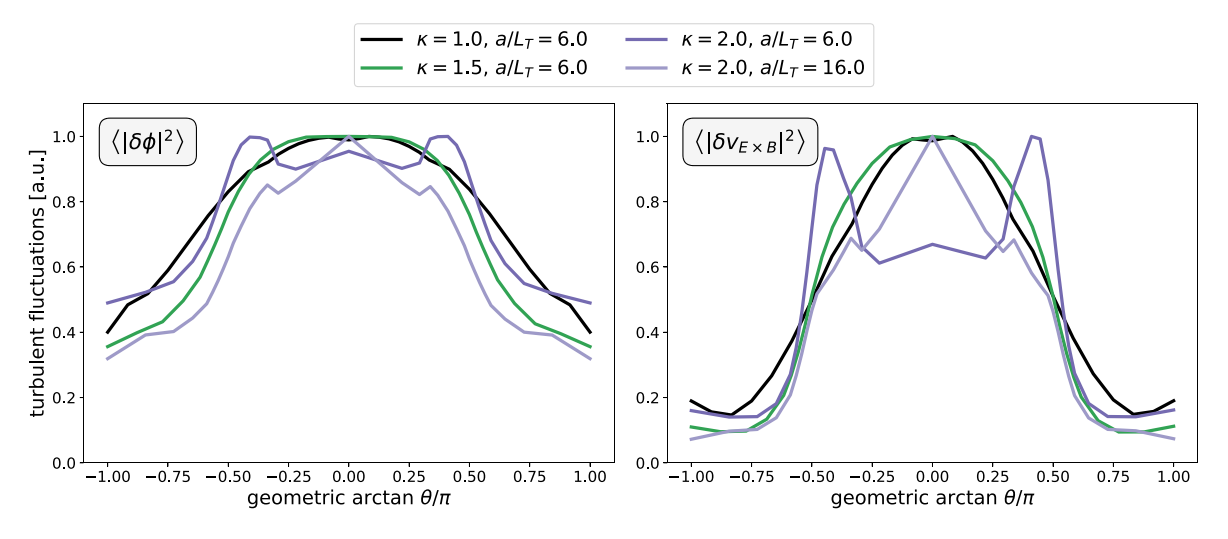


Figure 4. The poloidal distributions of the mean fluctuations for varying elongation and fixed gradient (solid), and for the highly elongated case with matched fluctuation level (shaded). Left: Electrostatic potential fluctuations. Right: $\mathbf{E} \times \mathbf{B}$ velocity fluctuations.

triangle pointing radially outwards, recently there has been a significant interest in NT [36]. Hence we include both positive triangularity (PT) and NT. Different from the variation of pure elongation we find that the turbulent fluctuations and heat flux do not depend as strongly on pure triangularity, figure 5. Motivated by this and figure 2, which showed that the variation of \mathcal{T}_{ν}^{ZF} seems to be more strongly impacted by the shaping than by the proximity to marginality, we keep the temperature gradient constant at $a/L_T=6.0$ throughout the triangularity scan.

Figure 6 shows the poloidal variation of \mathcal{T}_{ν}^{ZF} for different values of triangularity in the range between $\delta \in [-0.75, +0.75]$, where its radial variation is varied according to [27]

$$\frac{\partial \delta}{\partial r} = \frac{\delta}{\sqrt{1 - \delta^2}}. (17)$$

Two cross-section plots for $\delta = \pm 0.5$ are shown in figure 7 with $\mathcal{T}_{\nu}^{\text{ZF}}$ overlaid on the analyzed flux surface $\rho = 0.8$. As

was the case for elongation, \mathcal{T}_{ν}^{ZF} obtains local maxima close to those of poloidal curvature. For PT this includes the outboard midplane as a global maximum, with local maxima near the other two maxima of poloidal curvature. For NT, despite the curvature maximum at the inboard midplane, no local maximum of \mathcal{T}_{ν}^{ZF} is observed there. This is not surprising given that it is also the location of 'best' curvature. Further, no local maximum is found at the outboard midplane either. Finally, we observe that the fall off in \mathcal{T}_{ν}^{ZF} near its local maxima occurs faster for higher absolute values of triangularity.

The poloidal distributions of the turbulent fluctuations are shown in figure 8. For all values of triangularity the fluctuations generally peak on the outboard side, as expected. We notice that the $\mathbf{E} \times \mathbf{B}$ distributions develop a weak local minimum at the outboard midplane for $\delta < 0$. This effect is only seen for one of the NT cases in the potential fluctuations, and appears much weaker than in the $\mathbf{E} \times \mathbf{B}$ distributions.

We also note that while the fluctuations of the potential obtain their global *minimum* at the inboard midplane, the

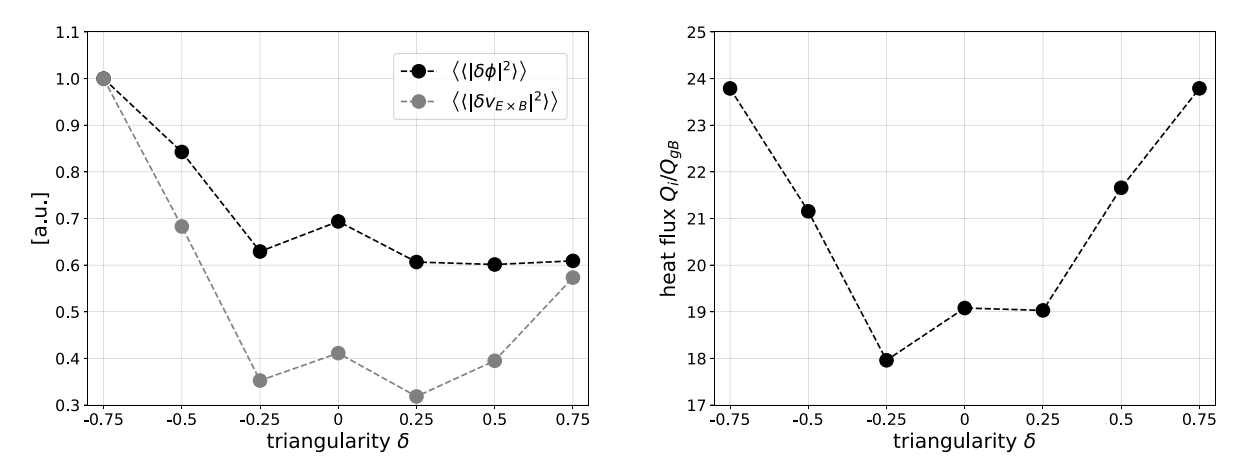


Figure 5. Different turbulence measures plotted against triangularity for fixed gradient drive of $a/L_T = 6.0$. Left: Different measures of poloidally averaged mean fluctuations. Right: The time-averaged heat flux.

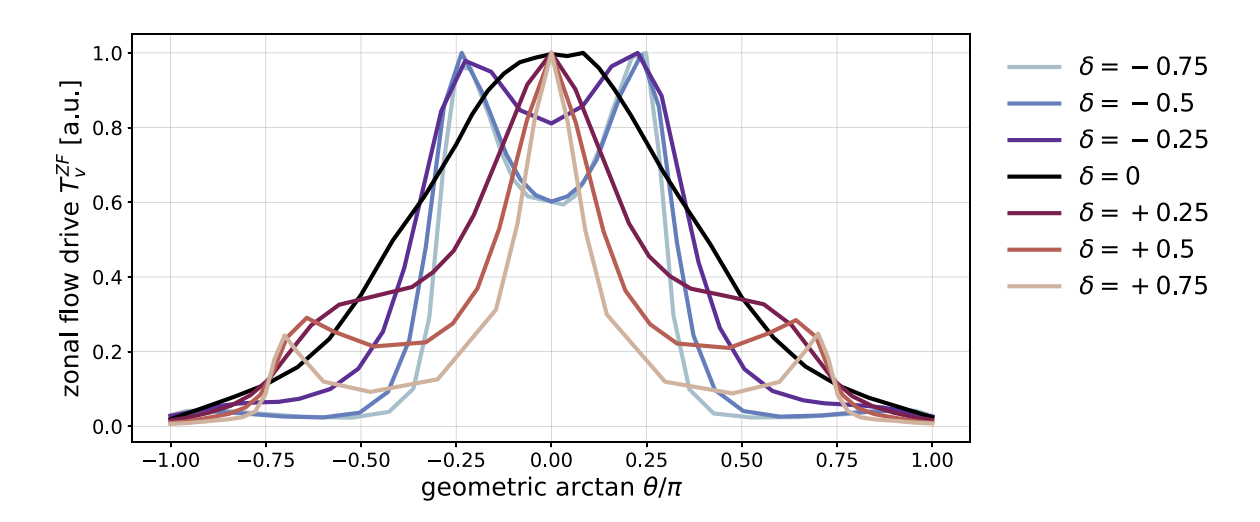


Figure 6. The distribution of ZF drive for varying triangularity at fixed temperature gradient $a/L_T = 6.0$.

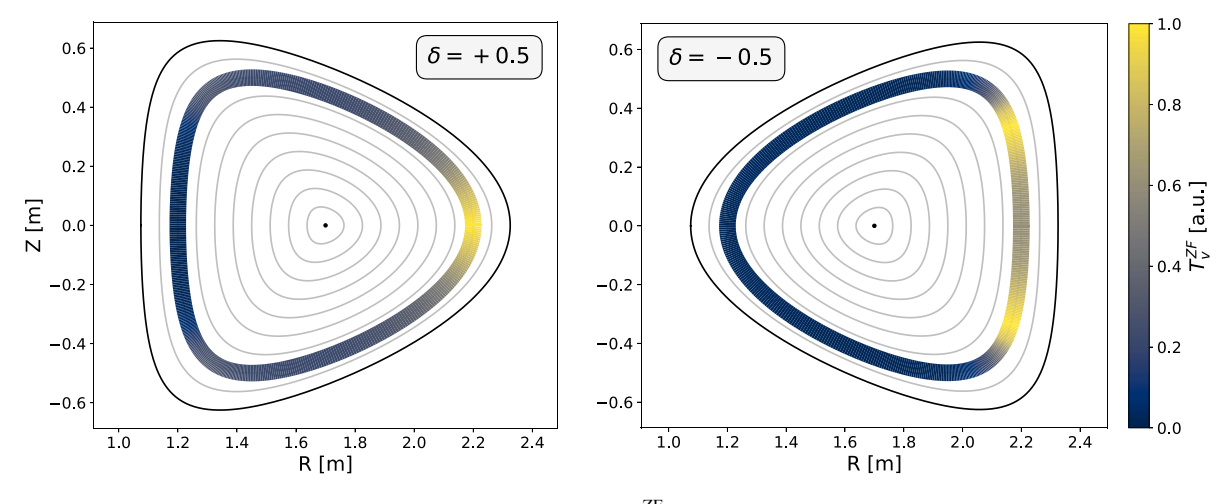


Figure 7. The toroidal cross-section of the simulated equilibrium with \mathcal{T}_{ν}^{ZF} is superimposed on the simulated flux surface $\rho = 0.8$. Each case has been normalized independently, so absolute values of \mathcal{T}_{ν}^{ZF} should not be compared between different equilibria. The radial width of the colored region is for illustrative purposes only. Left: $\delta = +0.5$. Right: $\delta = -0.5$.

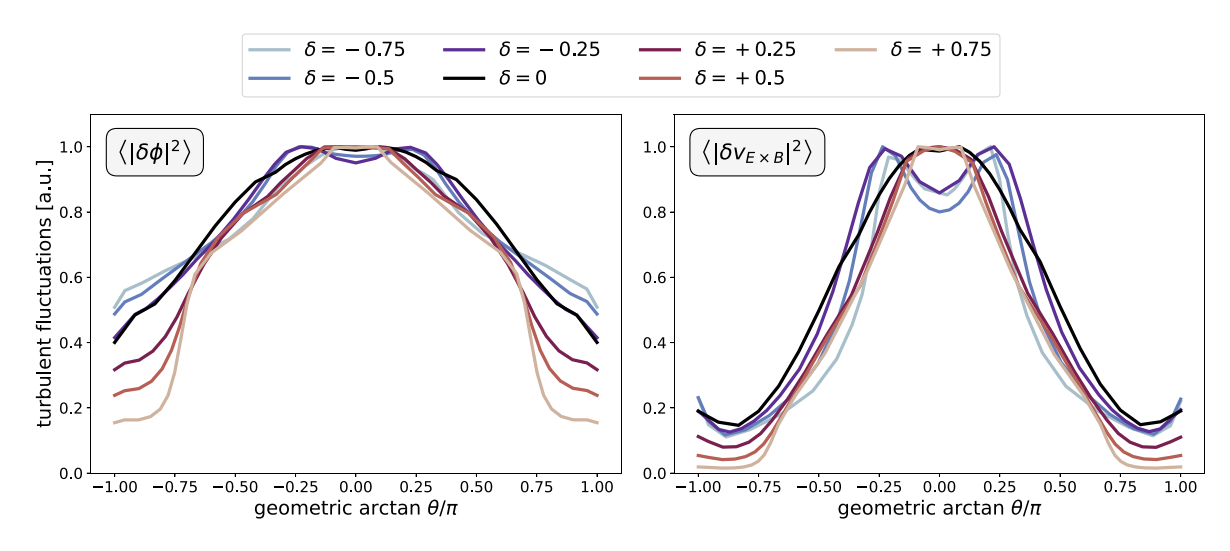


Figure 8. The poloidal distributions of the mean fluctuations for varying triangularity. Left: Electrostatic potential fluctuations. Right: $\mathbf{E} \times \mathbf{B}$ velocity fluctuations.

 $\mathbf{E} \times \mathbf{B}$ fluctuations can obtain a local maximum at this location. This local maximum is stronger the more negative the triangularity. Most importantly, however, as was the case for elongated equilibria in section 3.1, the envelopes of fluctuations show a distinctly different distribution from that of \mathcal{T}_{ν}^{ZF} in figures 6 and 7.

3.3. Aspect ratio

Aspect ratio alone has very little effect for circularly shaped cross-sections and therefore we do not show the results here. The general shape of the ZF drive does not change. The drive envelope merely becomes slightly wider at a small aspect ratio of A = 1.4 compared to A = 2.72 for the CBC, even when the effect of marginality is taken out by selecting the temperature gradient which matches the fluctuation level of the CBC. The poloidal distributions of the fluctuations are insensitive to aspect ratio alone.

3.4. Spherical tokamak shaping

Finally, we analyze the ZF drive for a typical equilibrium of a spherical tokamak like MAST-Upgrade. The results presented in the prior sections raise the question whether synergistic effects exist with combined shaping parameters. We use typical MAST-Upgrade values of A=1.4, $\kappa=2.0$, and $\delta=0.5$ [37, 38]⁴. Since these shaping parameters are all of stabilizing nature we raise the temperature gradient to $a/L_T=18$ to achieve similar fluctuation levels as for the other cases. Note that as before in the case of pure elongation, the chosen gradient, while large, ensures that we isolate the effect of the shaping rather than including additional effects based on the proximity to marginality. While linear studies of NT in STs predict detrimental transport from electromagnetic turbulence at the

power plant scale [40], it is nonetheless a valuable parameter space for validation and physics exploration of ST plasmas. Recently, the first ELM-free NT plasmas were successfully demonstrated on MAST-Upgrade [41]. For these reasons we also include the NT case here.

Figure 9 shows the results for spherical tokamaks equilibria with PT (top row) and NT (bottom row). Within each row, the left plot shows the distributions of both the ZF drive as well as the measures of the turbulent fluctuations, whereas the right plot shows the ZF drive mapped onto the relevant flux surface. For the PT case, similar to the cases of pure PT from section 3.2, local maxima of the drive occur at the top and bottom of the equilibrium where the poloidal curvature peaks. However, now no local maximum is observed at the outboard midplane as was the case for pure triangularity at standard aspect ratio. Instead, the transfer at the outboard midplane now represents a local minimum. We note that the poloidal curvature at the outboard midplane is now reduced due to the high elongation. Figure 10 shows that this effect is already observed at standard aspect ratio when PT and elongation are combined, suggesting that the effect of elongation on the drive distribution is stronger than that of triangularity. We note that the drive at the outboard midplane in figure 10 is not lowered as much as at small aspect ratio (figure 9 top), leading us to the conclusion that the additional reduction is due to lower aspect ratio.

The NT case at the bottom in figure 9 shows the same qualitative shape of $T_{\nu}^{\rm ZF}$ as for pure NT at A=2.72 (figure 6), though with an even stronger reduction of the ZF drive at the outboard midplane. Whereas pure NT with $\delta=-0.5$ at A=2.72 showed a reduction to $\sim 60\%$ of its maximum value at the outboard midplane, the drive at the outboard midplane here is reduced to $\sim 30\%$ of its maximum value.

3.5. Up-down asymmetry

The shaping cases considered thus far all retain up-down symmetry which describes the mirror symmetry of the flux

⁴ MAST-Upgrade equilibria also feature significant squareness which requires a reformulation of the Miller equations [39] and is thus neglected in this paper for simplicity.

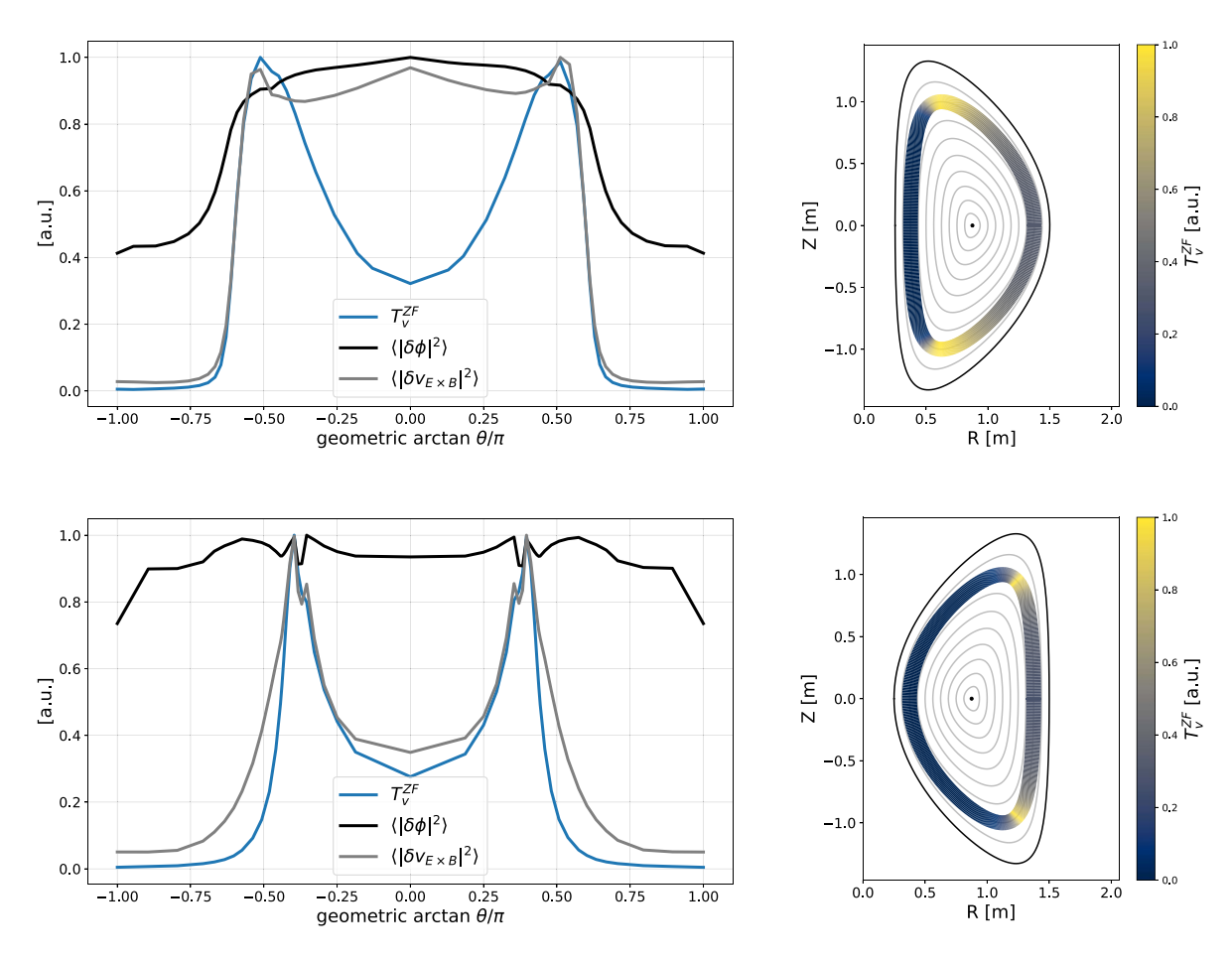


Figure 9. The poloidal distribution of the turbulent fluctuations and the nonlinear drive of zonal flows for a typical spherical tokamak equilibrium with A=1.4, $\kappa=2.0$, $\delta=\pm0.5$, and $a/L_T=18$. Note that in the cross section plots on the right the y-axis now coincides with the symmetry axis, indicating the compactness of these equilibria. Top: Spherical tokamak with positive triangularity. Bottom: Spherical tokamak with negative triangularity.

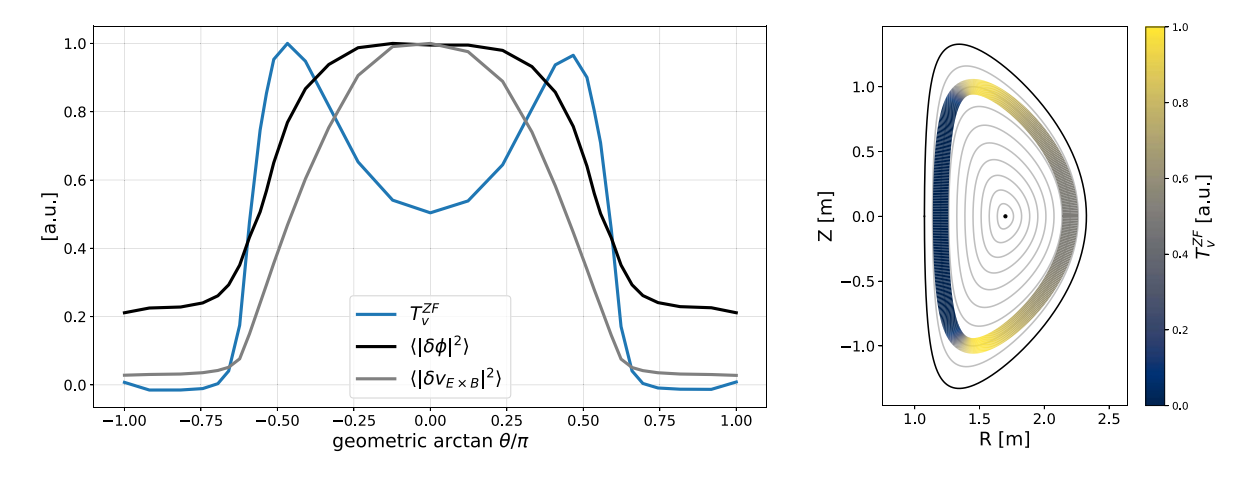


Figure 10. The poloidal distributions of ZF drive and turbulent activity for combined elongation and positive triangularity at standard aspect ratio $(A = 2.72, \kappa = 2.0, \delta = +0.5)$ are shown on the left. Here the chosen temperature gradient is $a/L_T = 16.0$ and is the one that matches the CBC fluctuation energy for pure elongation (see figure 1). The ZF drive mapped onto the flux surface is shown on the right.

surfaces across the midplane. Breaking up-down symmetry has strong implications, especially in the case considered here where the equilibrium toroidal flow and flow shear are assumed to vanish. In this case turbulent fluctuations are

unable to transport toroidal angular momentum radially for up-down symmetric equilibria due to a symmetry of the gyrokinetic equation [42]. The radial momentum flux from above the midplane cancels with the one from below. Hence,

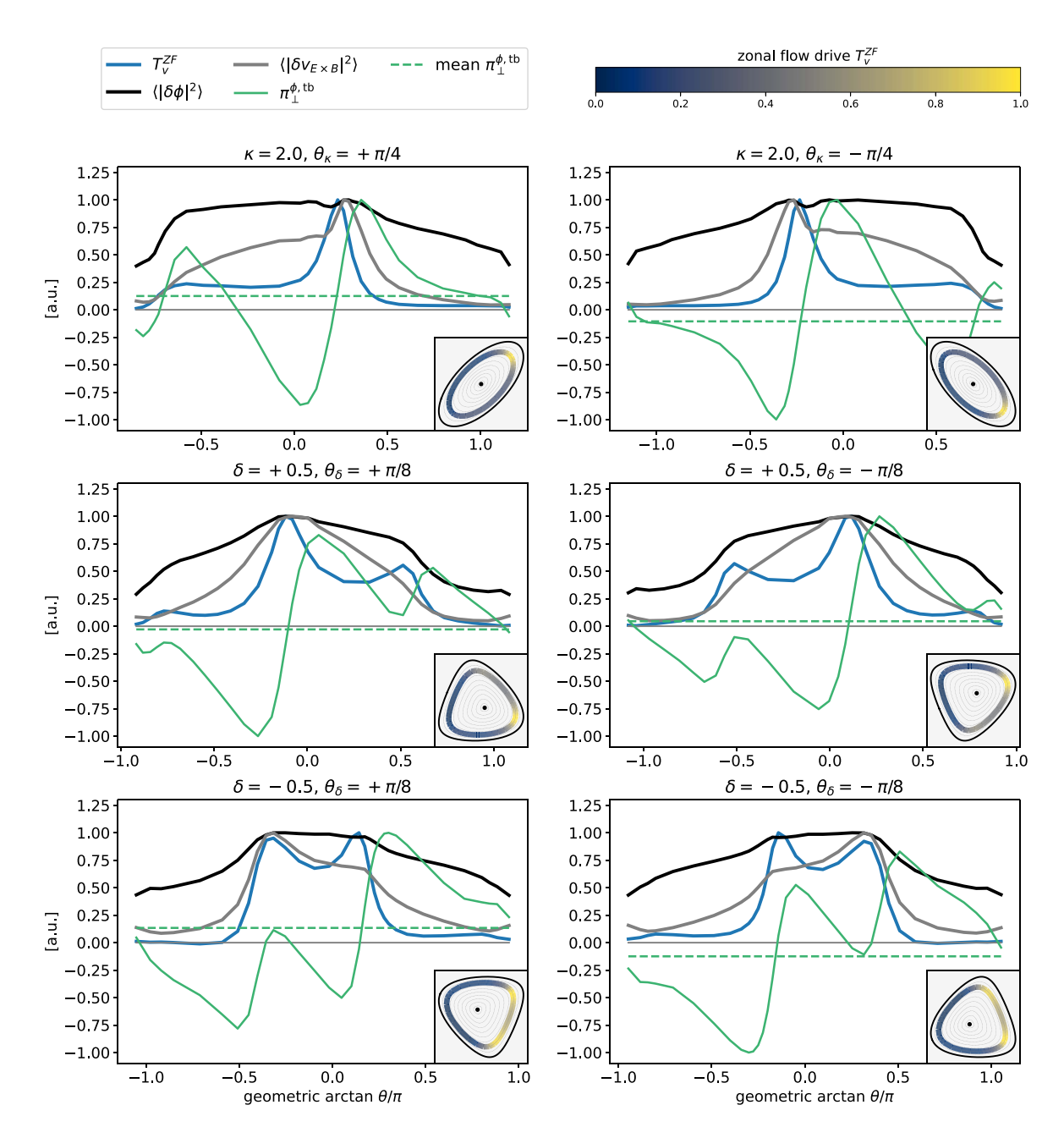


Figure 11. The poloidal distribution of zonal flow drive, turbulent fluctuations, and angular momentum transport for up–down asymmetry from tilting of Miller equilibria. For each we show results for positive and negative tilt angle to highlight the expected symmetry across $\theta = 0$. Top row: tilted elongation. Middle row: tilted positive triangularity. Bottom row: tilted negative triangularity. (Tilted elongation is evaluated at $a/L_T = 16.0$ and titled triangularity at $a/L_T = 6$).

rotation and rotation shear cannot be intrinsically generated from an initial stationary equilibrium. However, strongly updown asymmetric equilibria, as considered in this subsection, are able to transport toroidal angular momentum even in the absence of externally driven flow and flow shear [42].

A straightforward method of introducing up–down asymmetry is by tilting the Miller equilibria in the poloidal plane. This allows the equilibria to be expressed with generalized Miller equations which are implemented in GS2 [28, 29]. The two additional equilibrium parameters are θ_{κ} and θ_{δ} which describe the poloidal tilt angle of elongation and triangularity, respectively. We note that up–down asymmetric equilibria

which can be described by a single tilt angle, and thus retain a mirror symmetry in the poloidal plane, are a special case of up—down asymmetry since for small scale shaping (i.e. high Fourier mode shaping as opposed to the large scale, small Fourier mode shaping used here) the gyrokinetic equation possesses another symmetry which results in only small changes to the turbulent transport of momentum and energy [43].

Figure 11 shows the results for tilted elongation ($\theta_{\kappa} = \pm \pi/4$), as well as tilted positive and NT ($\theta_{\delta} = \pm \pi/8$). The broken symmetry of the flux-surface shape also breaks the symmetry of both the turbulent fluctuations and ZF drive. However, as expected with no flow or flow shear, both

are symmetric with respect to the sign of the tilt angle. Figure 11(top row) shows that the tilting of the elongated equilibria removes one of the two maxima and instead introduces a wider region of nearly constant transfer of $\sim 25\%$ of the maximum value. Similarly, the tilting of PT, shown in the middle row of figure 11, breaks the symmetry between the two local maxima, favoring the one at a larger major radius. The bottom row shows that the tilting of NT introduces only a small asymmetry between the two maxima.

Each plot also shows the poloidal distribution of the radial flux of the perpendicular component of toroidal angular momentum, $\pi_{\perp}^{\phi,\mathrm{tb}}(\theta)$ (called es_mom_flux_perp_dist in GS2), as well as its poloidal average. Most of the poloidal structure cancels and the net flux is much lower than the local maxima of the momentum flux. We also observe that $\pi_{\perp}^{\phi,\mathrm{tb}}$ shows no clear correlation with $\mathcal{T}_{\nu}^{\mathrm{ZF}}$ —in fact the locations where $\mathcal{T}_{\nu}^{\mathrm{ZF}}$ obtains maxima are often close to flux reversal points where the momentum flux locally vanishes. While the symmetry of both $\mathcal{T}_{\nu}^{\mathrm{ZF}}(\theta)$ and $\pi_{\perp}^{\phi,\mathrm{tb}}(\theta)$ is broken, the poloidal locations where perpendicular momentum is most strongly driven do not correspond to the locations where it is locally most strongly transported between flux surfaces, at least in the tilted cases considered here.

In experiments the symmetry of the gyrokinetic equation is usually broken due to non-zero equilibrium flow and flow shear as well as some amount of up-down asymmetric shaping. We have seen that the ZF drive is sensitive to this symmetry. We can therefore expect the ZF drive in experiments not only to peak away from the midplane, but asymmetrically so.

3.6. Transfer contributions

Additional insight into the origins of the observed poloidal ZF drive structure can be gained by omitting part of the summation in equation (15). Hence we define straightforwardly

$$\begin{split} \mathcal{T}_{v}^{ZF}\left(\theta,k_{x}\right) &= \sum_{k_{1x},k_{1y}} \mathcal{T}_{v}\left(k_{x},k_{y}=0,k_{1x},k_{1y},\theta\right),\\ \mathcal{T}_{v}^{ZF}\left(\theta,k_{1x}\right) &= \sum_{k_{x},k_{1y}} \mathcal{T}_{v}\left(k_{x},k_{y}=0,k_{1x},k_{1y},\theta\right),\\ \mathcal{T}_{v}^{ZF}\left(\theta,k_{1y}\right) &= \sum_{k_{x},k_{1x}} \mathcal{T}_{v}\left(k_{x},k_{y}=0,k_{1x},k_{1y},\theta\right), \end{split}$$

such that $\mathcal{T}_{v}^{\mathrm{ZF}}(\theta) = \sum_{k_{x}} \mathcal{T}_{v}^{\mathrm{ZF}}(\theta, k_{x})$ and analogously for $\mathcal{T}_{v}^{\mathrm{ZF}}(\theta, k_{1x})$ and $\mathcal{T}_{v}^{\mathrm{ZF}}(\theta, k_{1y})$. These modified transfer functions give spectrally resolved information of the poloidal distribution of the ZF drive. As such $\mathcal{T}_{v}^{\mathrm{ZF}}(\theta, k_{x})$ shows how the poloidal distribution of drive varies for ZFs of varying radial extent, whereas $\mathcal{T}_{v}^{\mathrm{ZF}}(\theta, k_{1x})$ and $\mathcal{T}_{v}^{\mathrm{ZF}}(\theta, k_{1y})$ highlight which turbulent scales transfer their energy to ZFs at each poloidal location. Here we analyze the equilibrium with pure elongation at standard aspect ratio from section 3.1 (A = 2.72; $\kappa = 2.0$; $\delta = 0.0$; $a/L_{T} = 6.0$).

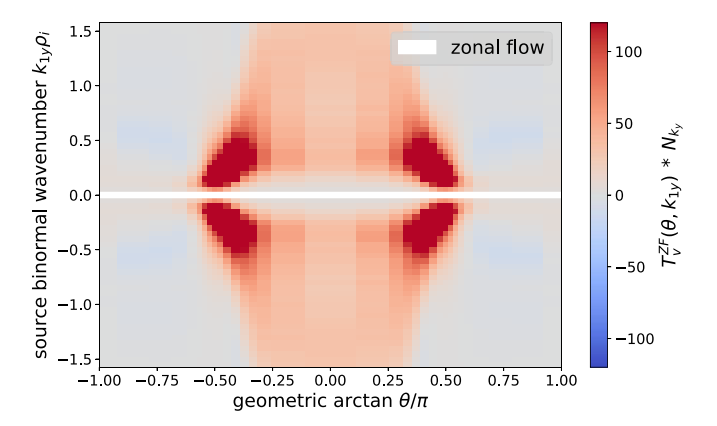


Figure 12. The drive from each binormal source mode at every poloidal location for pure elongation (A = 2.72; $\kappa = 2.0$; $\delta = 0.0$; $a/L_T = 6.0$).

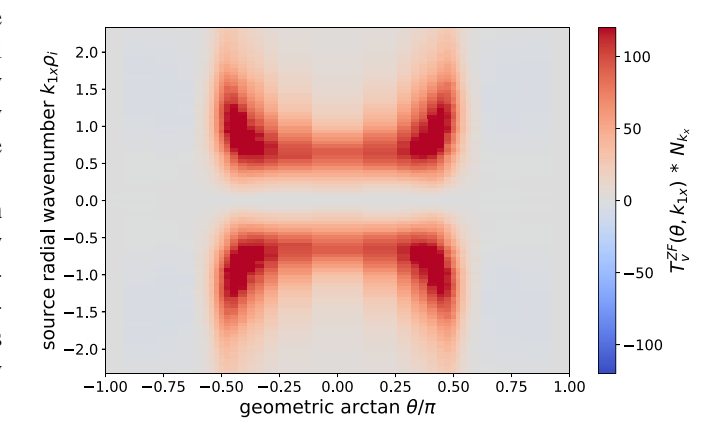


Figure 13. The drive from each radial source mode at every poloidal location for pure elongation (A = 2.72; $\kappa = 2.0$; $\delta = 0.0$; $a/L_T = 6.0$).

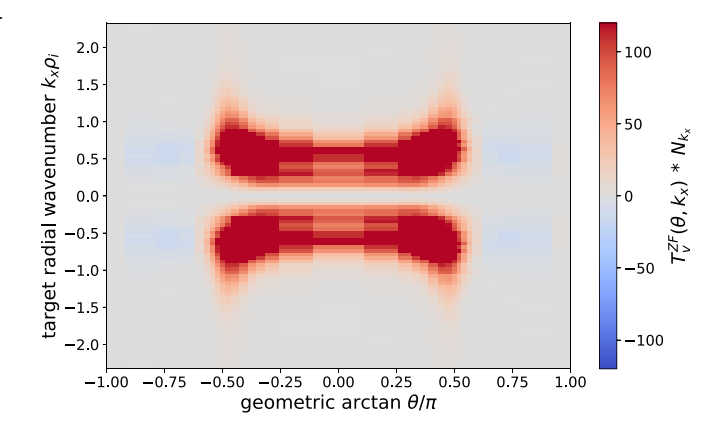


Figure 14. The zonal flow drive into each zonal mode of different radial wavenumber at every poloidal location for pure elongation $(A = 2.72; \kappa = 2.0; \delta = 0.0; a/L_T = 6.0)$.

Figure 12 shows $\mathcal{T}_{v}^{ZF}(\theta,k_{1y})$, giving information on which binormal eddy size is exchanging energy with ZFs at each poloidal location. The two local maxima near the top and bottom of the equilibrium, $|\theta| \sim 0.5$, from figures 2 and 3, now appear as two separate lobes in the θ - k_{1y} -space. These extend

from $0.1 \lesssim k_{1y}\rho_i \lesssim 0.5$ and feature a tilt, such that the drive furthest away from the midplane stems from the largest binormal source eddies. The drive towards the outboard midplane, away from the lobes, is broadly distributed in wavenumber space. We also note that on the inboard side two lobes appear with small negative energy exchange, i.e. where energy from ZFs is locally transferred back to the turbulence. These lobes are, however, small in comparison to the main lobes which drive ZFs.

Figures 13 and 14 show the poloidal distributions in radial wavenumber space, $\mathcal{T}_{v}^{\text{ZF}}(\theta, k_{1x})$ and $\mathcal{T}_{v}^{\text{ZF}}(\theta, k_{x})$, respectively. Figure 13 shows which radial eddy size is responsible for the drive at each poloidal location. We note that the drive towards the outboard midplane takes place across a relatively narrow range $0.3 \lesssim k_{1x}\rho_i \lesssim 0.9$. In contrast the drive near the top and bottom of the equilibrium extends to higher wavenumbers, with strong drive up to $k_{1x}\rho_i \sim 1.6$. The distinct poloidal structure from figures 2 and 3 is therefore also present at many of the individual scales. Figure 14 shows which zonal modes (differentiated by their different radial scales) receive energy at each poloidal location. A similar structure as in figure 13 appears. However only ZFs with $k_{1x}\rho_i \lesssim 1.1$ receive significant energy. As in figure 13, the drive at the outboard midplane is more localized in wavenumber space to $k_{1x}\rho_i \sim 0.5$, whereas a wider range of zonal structures receive energy near the top and bottom of the equilibrium, resulting in the local maxima of the total drive in these locations.

3.7. How does geometry and curvature affect the ZF drive distribution?

The overarching and striking result from the previous sections is the influence of curvature on the ZF drive. Visually in the mapping of the drive on the poloidal cross-section, drive maxima appear near those of poloidal curvature with a tendency to be shifted towards the bad curvature side.

One way in which curvature enters the turbulence dynamics is through the field line curvature $\kappa_{\mathbf{b}} = \mathbf{b} \cdot \nabla \mathbf{b}$, which can naturally be decomposed into its normal component $\kappa_n = \mathbf{n} \cdot \boldsymbol{\kappa}$ and its geodesic component $\kappa_g = (\mathbf{b} \times \mathbf{n}) \cdot \boldsymbol{\kappa}$. Here $\mathbf{n} = \nabla \psi / |\nabla \psi|$ is the flux surface normal [44]. For linear ITG physics it is not the normal curvature but the so-called (magnetic) drift curvature which describes the strength of the curvature drive and distinguishes regions of good and bad curvature. For modes with zero radial wavenumber, which are usually the most strongly driven ones, its poloidal variation is given by

$$\kappa_d \propto B^{-1} (\mathbf{b} \times \nabla \alpha) \cdot \boldsymbol{\kappa}.$$
(18)

Note that this is equal to the α -component of the curvature drift. Geodesic curvature can impact the linear [45, 46] and nonlinear damping [47] of ZFs. Other geometric quantities which enter the gyrokinetic equation and thus affect the turbulence are the field strength B, and the metric components $g^{\psi\psi} = |\nabla\psi|^2$, $g^{\psi\alpha} = \nabla\psi \cdot \nabla\alpha$, $g^{\alpha\alpha} = |\nabla\alpha|^2$. The geodesic curvature is equal to the radial component of the magnetic drift. Since we consider electrostatic equilibria, the

 α -components of the curvature and grad-B drift are also identical. All six independent geometric quantities and the surface curvatures are shown alongside \mathcal{T}_{v}^{ZF} in figure 15. The surface curvatures, the toroidal curvature κ_1 and poloidal curvature κ_2 , were calculated analytically from the Miller equilibrium equations (see appendix D). We confirm the previous observation that ZF drive maxima are near those of poloidal curvature. While none of the geometric quantities appear directly correlated with the ZF drive, the drift curvature κ_d features a similar structure on the outboard side. The drift curvature can be varied without changing the poloidal curvature by modifying the safety factor. To understand why we note that (1) if $\nabla \psi$ and $\nabla \alpha$ were exactly orthogonal, the drift curvature would correspond to the normal curvature, and (2) that the normal curvature is related to the principle curvatures via [48, theorem 42.1]

$$\kappa_n = \kappa_1 (\cos \xi)^2 + \kappa_2 (\sin \xi)^2, \qquad (19)$$

where $\xi = \arctan(1/q)$ is the pitch angle, i.e. the angle between the field line and the toroidal direction. From this we conclude that the coupling between the drift curvature and the poloidal curvature can be reduced by decreasing the pitch angle ξ , i.e. by increasing the safety factor q.

In figure 16 the results for the CBC safety factor q = 1.4 are compared to those with increased safety factor of q = 4. Indeed, the drift curvature now follows mostly the toroidal curvature and therefore only exhibits a very weak variation on the outboard side. The ZF drive, while somewhat weakened, still features its characteristic structure.

We conclude from this that none of the geometric quantities appear to be able to explain the geometric variation of the ZF drive individually. Gaining further insight into how exactly geometry affects the poloidal distribution of the ZF drive is a non-trivial exercise due to the inherently nonlinear nature of the dynamics, and is therefore outside the scope of this work.

Despite this, the poloidal curvature, while lacking a physical explanation at this point, does appear to be a good indicator for the general structure, and we shall use this observation to test simple transfer proxies in the next section.

3.7.1. Transfer proxies. Given the observations from the previous sections that the ZF drive is influenced both by poloidal curvature and turbulent activity we test the quality of a simple proxy function of the form $\langle \delta | v_{E \times B} |^2 \rangle * |\kappa_2|$. Since this proxy still relies on the nonlinear results and would therefore not offer any meaningfully faster evaluation than $\mathcal{T}_{v}^{\mathrm{ZF}}$ itself, we also test the linear proxy of $|\phi^{\mathrm{linear}}(k_{\mathrm{v}}^{\mathrm{max}})| * |\kappa_2|$. Here $|\phi^{\text{linear}}(k_v^{\text{max}})|$ represents the linear mode envelope at the final time step of the corresponding linear simulation for the most unstable mode. The results for many of the presented cases are shown in figure 17. Both proxies recreate the qualitative shape of the ZF drive distribution and the location of local maxima reasonably well. Often the proxies are too strongly influenced by the curvature information. This is especially the case for the nonlinear proxy.

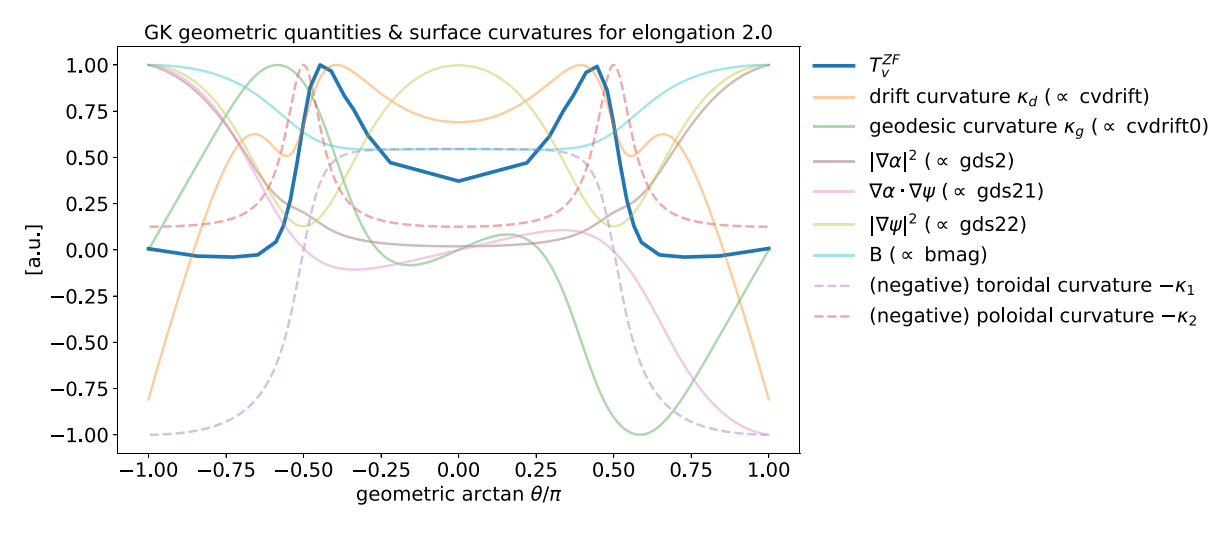


Figure 15. The poloidal variations of the gyrokinetic geometric quantities alongside the zonal flow drive for the elongated equilibrium with q=1.4. Also shown are the principal curvatures of the flux surface. Where applicable the corresponding GS2 output names are listed in the legend.

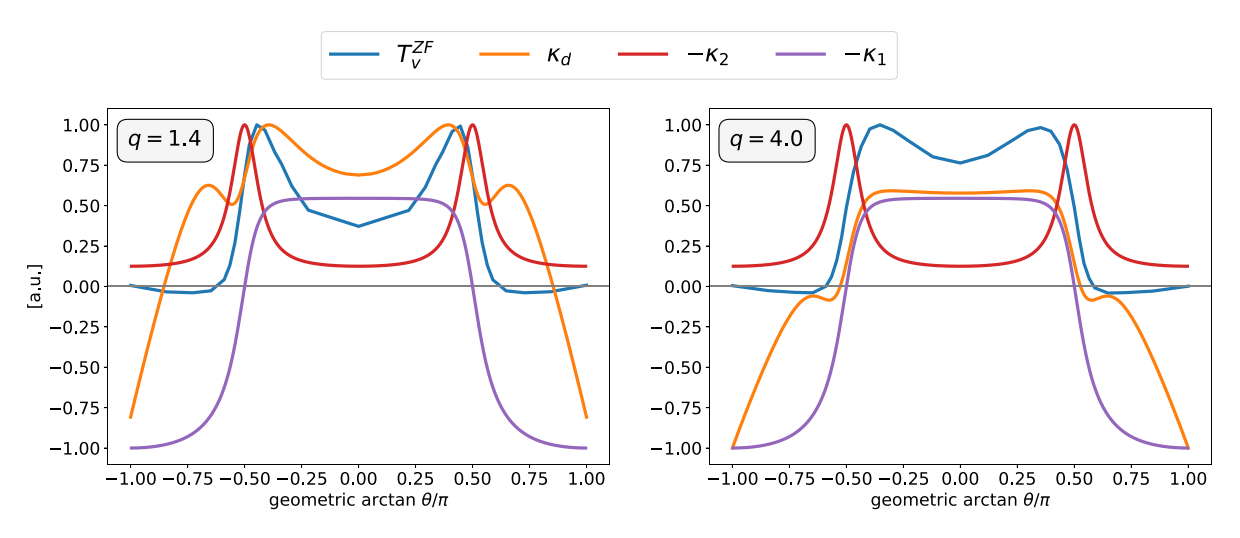


Figure 16. The surface curvatures, drift curvature κ_d , and ZF drive for varying safety factors. Left: the results for the CBC value of q = 1.4 are shown. Right: the result for a shallow pitch angle, q = 4.0, where most of the normal curvature is provided by the toroidal curvature.

4. Summary and discussion

In this paper we presented the first analysis of the poloidal variation of ZF drive for strong axisymmetric shaping described by Miller equilibria. We first examined the separate influence of the three major shaping parameters: aspect ratio, elongation, and triangularity. Compared to circular plasma shaping where the drive of ZFs obtains a single maximum at the outboard midplane, this maximum splits as elongation is introduced. Two local maxima develop near the locations of maximum poloidal curvature and tend to be shifted towards the bad curvature side.

The analysis of triangularity shows a clear asymmetry for the sign of triangularity. PT develops one global maximum at the outboard midplane with two local maxima at the two inner corners of the triangle. NT develops two local maxima at the outer corners but shows negligible drive at the inner corner, where the potential fluctuations are also minimal. Typical spherical tokamak equilibria with low aspect ratio, high elongation, and high triangularity showed strong drive near the top and bottom of the equilibrium. The transfer at the outboard midplane is shown to be small in comparison, approaching inboard midplane levels. We identified this to be due to the dominant effect of elongation over triangularity. We also showed that the Reynolds stress becomes up-down asymmetric for up-down asymmetric equilibria created by tilting of elongated or triangular equilibria. This is relevant for experiments where the up-down symmetry of the gyrokinetic equation is usually broken by equilibrium flow and flow shear as well as shaping. An asymmetric poloidal distribution of the Reynolds stress which peaks away from the midplane can be expected in realistic plasma shaping.

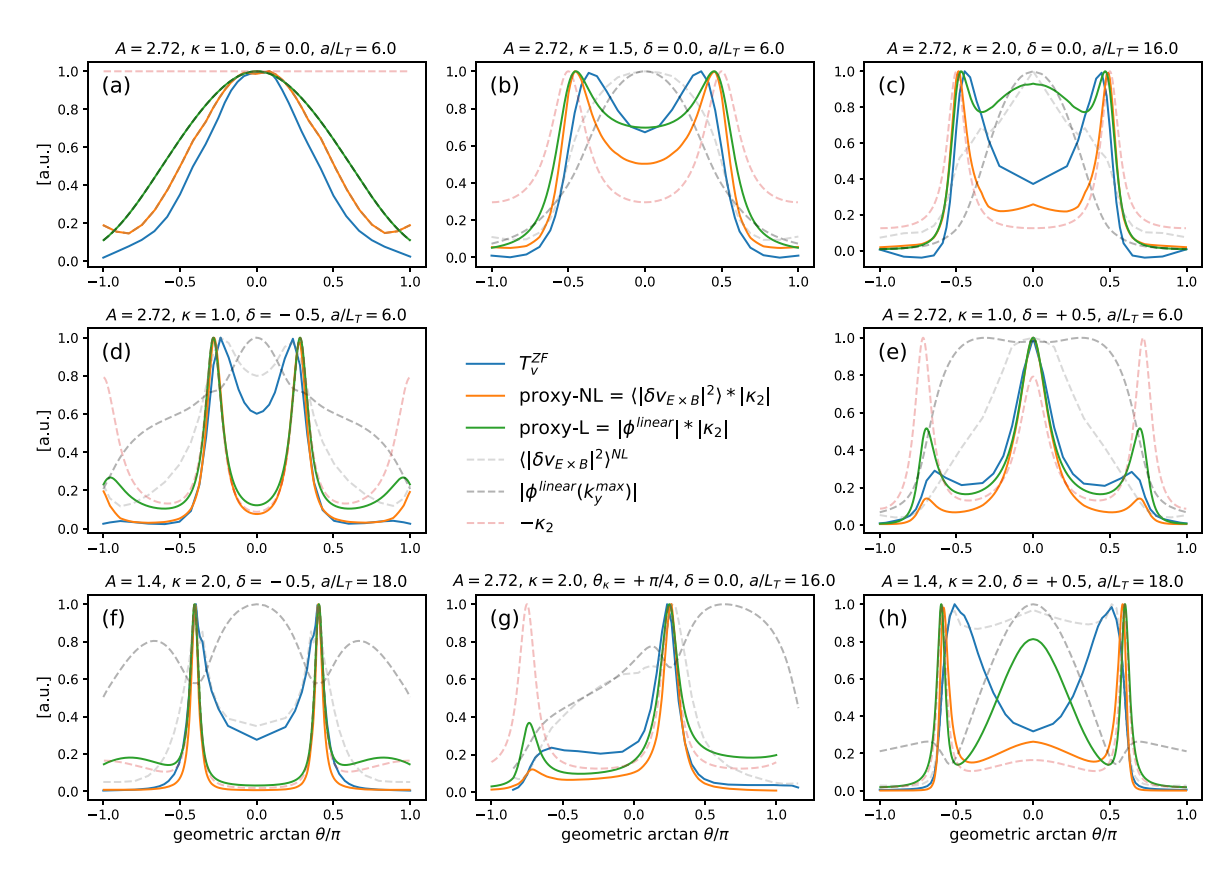


Figure 17. A proxy for \mathcal{T}_{ν}^{ZF} based on linear quantities in green and one based on the nonlinear fluctuation envelope in orange. The contributing quantities are shown in light dashed lines. The configurations are (a) 'CBC', (b) 'slightly-elongated-CBC', (c) 'elongated-CBC', (d) 'NT-CBC', (e) 'PT-CBC', (f) 'elongated-NT-ST', (g) 'tilted-elongation', (h) 'elongated-PT-ST'.

These results have important implications for the experimental interpretation of ZF drive measurements which are typically performed at the outboard midplane. First, extrapolation from this limited range to a global phenomenon *must* consider the clear distinction between turbulence power and ZF drive distribution, especially in strongly shaped plasmas. Second, relative changes in the drive at the midplane between experiments may not be indicative of the change in the total ZF drive in cases where the plasma shape also changed. However, the ZF drive envelopes and proxies thereof presented in this paper could be used to get a fairly inexpensive estimate for the total drive from a single poloidal (e.g. midplane) measurement and could thus render a comparison between experiments with different shaping possible again.

Given these results one wonders about the underlying physical mechanism which results in strong nonlinear coupling at the locations of locally maximal poloidal curvature. Recent work showed that the poloidal variation of the mean $\mathbf{E} \times \mathbf{B}$ shearing rate also exhibits bifurcations when the shaping is changed from circular to non-zero triangularity [19]. Based on the observed asymmetry in the shearing rate for different upper and lower triangularity, it was suggested that this asymmetry about the outboard midplane could also be present in the Reynolds stress. We note, however, that our study does not

feature a background flow shear, but rather an asymmetry in the Reynolds stress is observed purely based on how geometry itself affects the nonlinear turbulence dynamics. Prior to a confinement transition a strong background flow shear might be absent. Further, it is worth noting that the tilt angle of the turbulent eddies, and thus the Reynolds stress, must not be proportional to the equilibrium shearing rate since shearing could transition poloidally from a regime where it mostly tilts and elongates turbulent eddies into one where it breaks them apart into smaller ones.

It is not clear whether our observed splitting of the maxima, e.g. for elongation, is caused by a relative increase of the drive near the top and bottom of the device or by a relative decrease at the outboard midplane, or by both. To answer this question the kinetic energy transfer must be normalized to the mean ZF fluctuation level and then be compared between different simulations. However, the ZF level is observed to be sensitive to changes in the flux surface shaping, likely due to small changes in numerical dissipation. For some cases the ZF level is only observed to be quasi-stationary, rendering such a normalization difficult to realize. Thus, such a comparison requires a more careful analysis of the mechanisms which affect the mean ZF level and is outside the scope of this paper.

The perhaps unexpected sensitivity of the ZF drive envelope raises many new questions. These include the effect of electromagnetic instabilities, the poloidal variation of the corresponding Maxwell stress, and the net effect on ZF generation when taken in combination with the Reynolds stress. This is particularly relevant for the spherical tokamak equilibria presented here since future spherical tokamaks such as STEP [49] aim to operate at high plasma beta to leverage one of the key benefits of small aspect ratio. The experimentally driven development of alternative confinement regimes in such equilibria requires knowledge of the full electromagnetic ZF drive envelope. One might also wonder how or if the presented results change for higher fidelity gyrokinetic simulations which include gyrokinetic electrons or collisions. Other interesting questions include other symmetry breaking mechanisms of the gyrokinetic system such as non-zero equilibrium flow and flow shear even for up-down symmetric shaping [42] which is known to shift the ballooning angle away from the outboard midplane. Finally, given the observed sensitivity to geometric details one wonders how the drive of ZFs behaves in stellarator equilibria where smaller scale changes of the geometric quantities are ubiquitous. Efforts to explore these avenues have been initiated.

Data availability statement

The data for this paper is available for download on Zenodo and can be found at https://doi.org/10.5281/zenodo.17431814 [50].

Acknowledgments

We are grateful for helpful discussions with Stephen Biggs–Fox, Bailey Cook, Simon Freethy, Michael Barnes and Pat Diamond. This work was supported by the Engineering and Physical Sciences Research Council (EP/S022430/1) and (EP/R034737/1). This work used the ARCHER2 UK National Supercomputing Service (www.archer2.ac.uk) (Grant Number EP/X035336/1). We also acknowledge the use of computing resources on the Viking supercomputer at the University of York.

Appendix A. Linear resolution

For the linear results shown in this paper we use a minimum of $N_{\theta} = \text{ntheta} = 192$ parallel grid points per poloidal turn, over $N_{\text{poloidal}} = 3$ (nperiod = 2) poloidal turns. The velocity resolution is given by $N_{\lambda} = 113$ (ngauss = 8) and $N_{\varepsilon} = \text{negrid} = 32$. The time step is $\Delta t = 0.15 \, a/v_{th}$. Convergence was checked for the most strongly shaped cases within each shaping domain. Simulations were considered converged when there were no visible variations in the growth rate spectra $\gamma(k_{\nu})$ upon doubling the parallel grid and number

of trapped particles (ntheta), the energy grid (negrid), the number of passing particles (ngauss), the simulation time (max_sim_time), as well as halving the time step (delt) and extending the parallel domain. The binormal wavenumber is scanned in the range $0.1 \lesssim k_y \rho_i \lesssim 1.0$, ensuring that the binormal wavenumber with the maximum growth rate is captured. Simulations are performed for zero ballooning angle $\theta_0 = 0$ and quantities of the fastest growing mode within the chosen k_y -range are shown for each case.

Appendix B. Nonlinear resolution

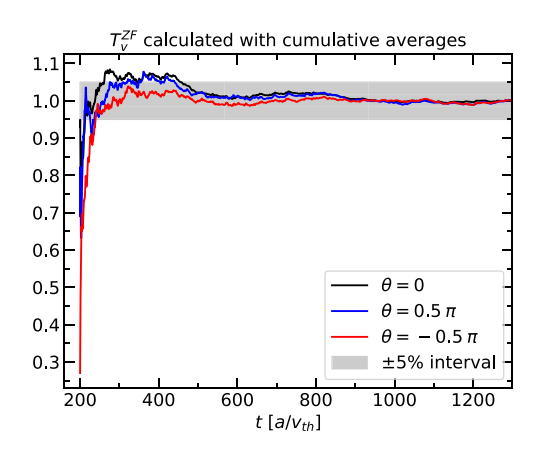
Noting that the radial length of the simulation box is quantized for finite magnetic shear [32], we use an approximately square simulation box with $L_v = 125.66 \rho_i$ (y0 = -0.05) and $L_x =$ $128.20\rho_i$ (jtwist = 5), and with minimum resolutions $N_x =$ nx = 128 and $N_y = ny = 64$. These resolutions correspond to a perpendicular grid spacing of $\Delta x = 1.01 \rho_i$ and $\Delta y = 0.99 \rho_i$. After de-aliasing with the 3/2 rule [51, 52], the radial and binormal wavenumbers are resolved in the range $-2.058 \le$ $k_x \rho_r \leq 2.058$ and $0.0 \leq k_y \rho_r \leq 1.05$ with grid cell sizes of $\Delta k_x \rho_r \sim \Delta k_y \rho_r \sim 0.05$. The minimum parallel resolution used is $N_{\theta} = \text{ntheta} = 32$. The minimum velocity space resolution is $N_{\lambda} = 47$ (npassing = 15) and $N_{\varepsilon} = \text{negrid} = 16$, where $\lambda = \mu_s/\varepsilon_s$ is the trapping parameter with the magnetic moment $\mu_s = m_s v_\perp^2 / (2B)$. The required resolutions were determined by checking that the heat flux, the spectra of the electrostatic potential, and the poloidal zonal flow (ZF) drive envelope do not change meaningfully for a 50% increase in any of the grid resolution or under halving of the cfl parameter.

Appendix C. Nonlinear coupling convergence

Along with the heat flux and fluctuation spectra, the convergence of the \mathcal{T}_{ν}^{ZF} was also checked both against doubling in any of the grid resolutions and halving of the cfl parameter at the most extreme cases within each shaping domain (not shown).

The nonlinear convergence with respect to the number of realizations (time points) was checked by calculating cumulative ensemble averages. The results for three somewhat arbitrarily selected poloidal locations are shown on the left in figure C1. For time points $t \gtrsim 500a/v_{th}$ the changes are < 5%, showing sufficient convergence. Note that the time stepping did not change during this phase such that spacing in t is representative of spacing in realizations.

To check that the distributions are stationary and not dominated by individual large scale events \mathcal{T}_{v}^{ZF} is averaged over disjoint intervals of length $t_{\text{interval}} = 250 \, a/v_{\text{th}} \, (N_{\text{interval}} = 800 \, \text{time points})$ within the saturated period of the simulations. Figure C1 shows that this criterion is satisfied as virtually no variations in the poloidal distributions are visible between the disjoint intervals.



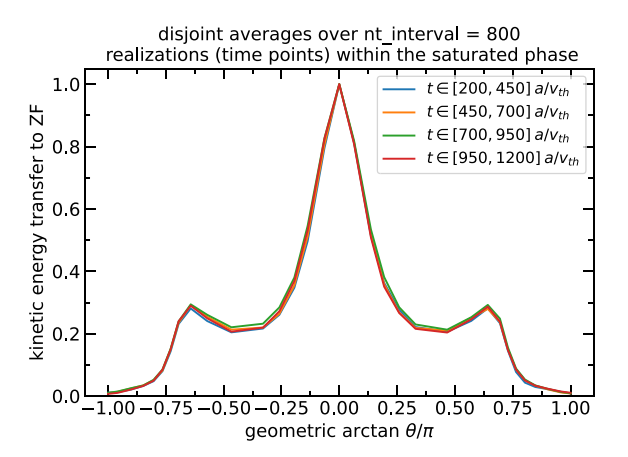


Figure C1. Convergence of nonlinear coupling for $\mathcal{T}_{\nu}^{\mathrm{ZF}}$. Left: kinetic energy transfer to zonal flows calculated with cumulative averages within the saturated phase to test the convergence of the nonlinear coupling at three selected poloidal locations. Each curve is normalized to its final value since the differences of the final state were established in figure 8. Right: zonal flow drive $\mathcal{T}_{\nu}^{\mathrm{ZF}}$ averaged over disjoint intervals of length $t_{\mathrm{interval}} = 250a/v_{\mathrm{th}}$ within the saturated period of the simulations. The case shown here is A = 2.72; $\kappa = 1.0$; $\delta = +0.5$; $a/L_T = 6.0$.

Appendix D. Analytic expressions for principal curvatures in Miller equilibria

If the coordinate curves on a surface are lines of curvatures, as is the case for an axisymmetric torus⁵, then the principle curvatures are given by

$$\kappa_1 = \frac{b_{\phi\phi}}{g_{\phi\phi}} \quad \text{and} \quad \kappa_2 = \frac{b_{\theta\theta}}{g_{\theta\theta}}, \tag{D.1}$$

where

$$g_{\alpha\beta} = \mathbf{x}_{\alpha} \cdot \mathbf{x}_{\beta} \tag{D.2}$$

are the coefficients of the first fundamental form and

$$b_{\alpha\beta} = \mathbf{x}_{\alpha\beta} \cdot \mathbf{n} \tag{D.3}$$

are the coefficients of the second fundamental form [48]. Here

$$\mathbf{n} = \frac{\mathbf{x}_{\phi} \times \mathbf{x}_{\theta}}{|\mathbf{x}_{\phi} \times \mathbf{x}_{\theta}|} \tag{D.4}$$

is the surface normal and the partial derivatives of the position vector $\mathbf{x}(\theta, \phi)$ are defined through [48]

$$\mathbf{x}_{\alpha} = \frac{\partial \mathbf{x}}{\partial \alpha}$$
 and $\mathbf{x}_{\alpha\beta} = \frac{\partial^2 \mathbf{x}}{\partial \alpha \partial \beta}$, (D.5)

and $\alpha, \beta \in \{\phi, \theta\}$. For up–down symmetric Miller equilibria the position vector is given by

$$\mathbf{x}(\theta,\phi) = \begin{bmatrix} R(\theta)\cos(\phi) \\ R(\theta)\sin(\phi) \\ Z(\theta) \end{bmatrix}, \tag{D.6}$$

$$R(\theta) = R_0 + r\cos(\theta + \delta\sin(\theta)), \qquad (D.7)$$

$$Z(\theta) = \kappa r \sin(\theta), \tag{D.8}$$

where $\delta \equiv \arcsin \delta_M$. The calculation to obtain κ_1 and κ_2 is simple but tedious and has therefore been performed with a computer algebra system (Mathematica 12). The final result is given by the expressions

$$\kappa_1(\theta, \phi) = \frac{a(\theta, \phi)}{b(\theta, \phi)} \tag{D.9}$$

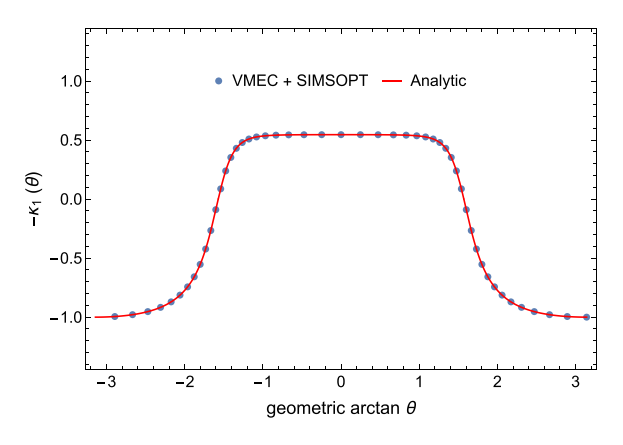
for the toroidal curvature, where

$$\begin{split} a\left(\theta,\phi\right) &= 2\kappa\cos\left(\theta\right), \\ b\left(\theta,\phi\right) &= c\left(\theta,\phi\right)\left(r\cos\left(\delta\sin\left(\theta\right) + \theta\right) + R_0\right), \\ c\left(\theta,\phi\right) &= \left[\delta^2 + 2\kappa^2 + \left(\delta^2 + 2\kappa^2\right)\cos\left(2\theta\right) - \frac{1}{2}\delta^2\cos\left(2\delta\sin\left(\theta\right)\right) \right. \\ &- \delta^2\cos\left(2\left(\delta\sin\left(\theta\right) + \theta\right)\right) - \frac{1}{2}\delta^2\cos\left(2\delta\sin\left(\theta\right) + 4\theta\right) \\ &+ 4\delta\cos\left(\theta\right) - 2\delta\cos\left(2\delta\sin\left(\theta\right) + \theta\right) \\ &- 2\delta\cos\left(2\delta\sin\left(\theta\right) + 3\theta\right) - 2\cos\left(2\left(\delta\sin\left(\theta\right) + \theta\right)\right) + 2 \right]^{1/2}, \end{split}$$
(D.10)

and the poloidal curvature is given by

$$\kappa_2(\theta,\phi) = \frac{d(\theta,\phi)}{e(\theta,\phi)},\tag{D.11}$$

⁵ This becomes apparent from the fact that $g_{\phi\theta} = b_{\phi\theta} = 0$ [48, theorem 41.3, see also section 43].



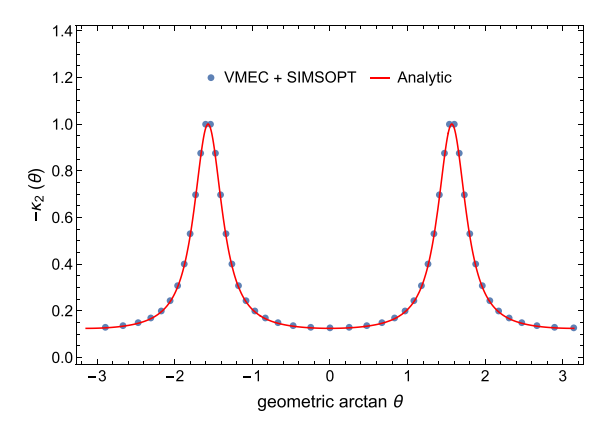


Figure D1. Comparison of the poloidal distributions of the principal curvatures from the analytic formulae (red) and the numerical calculation from the general three-dimensional codes SIMSOPT & VMEC (blue). (a) Shows a comparison for the toroidal curvature κ_1 and (b) for the poloidal curvature κ_2 . Here A=2.72, $\kappa=2.0$, $\delta=0.0$, and r/a=0.8.

where

$$\begin{split} d(\theta,\phi) &= \kappa f(\theta,\phi)\,,\\ f(\theta,\phi) &= \left(3\delta^2 + 8\right)\cos\left(\delta\sin\left(\theta\right)\right) + \delta g\left(\theta,\phi\right)\,,\\ g\left(\theta,\phi\right) &= 4\cos\left(\theta - \delta\sin\left(\theta\right)\right)\\ &\quad + \delta\cos\left(2\theta - \delta\sin\left(\theta\right)\right) + 8\cos\left(\delta\sin\left(\theta\right) + \theta\right)\\ &\quad + 3\delta\cos\left(\delta\sin\left(\theta\right) + 2\theta\right) + 4\cos\left(\delta\sin\left(\theta\right) + 3\theta\right)\\ &\quad + \delta\cos\left(\delta\sin\left(\theta\right) + 4\theta\right)\,,\\ e\left(\theta,\phi\right) &= 2rh\left(\theta,\phi\right)k\left(\theta,\phi\right)\,,\\ h\left(\theta,\phi\right) &= \left[4\left(\delta^2 + 2\kappa^2\right)\cos(2\theta) - 2l(\theta,\phi) + 16\delta\cos(\theta)\right]^{1/2}\,,\\ l(\theta,\phi) &= -2\delta^2 - 4\kappa^2 + \delta^2\cos(2\delta\sin(\theta))\\ &\quad + \delta^2\cos(2\delta\sin(\theta) + 4\theta) + 2\left(\delta^2 + 2\right)\cos(2(\delta\sin(\theta) + \theta))\\ &\quad + 4\delta\cos(2\delta\sin(\theta) + \theta) + 4\delta\cos(2\delta\sin(\theta) + 3\theta) - 4\,,\\ k(\theta,\phi) &= \cos^2(\phi)\sin^2(\delta\sin(\theta) + \theta)(\delta\cos(\theta) + 1)^2\\ &\quad + \sin^2(\phi)\sin^2(\delta\sin(\theta) + \theta)(\delta\cos(\theta) + 1)^2\\ &\quad + \kappa^2\cos^2(\theta). \end{split} \tag{D.12}$$

These equations are stated for completeness but are cumbersome and do not give particular insight. However, we notice that in the circular limit where $\kappa = 1.0$ and $\delta = 0$ we recover the known formulae for the circular torus [48, p 135]

$$\kappa_1 = \pm \frac{\cos(\theta)}{r\cos(\theta) + R_0} \quad \text{and} \quad \kappa_2 = \pm \frac{1}{r}.$$
(D.13)

The surface curvatures for the up-down asymmetric cases were obtained analogously by replacing equations (D.7) and (D.8) with the equations for the tilted Miller equilibria from [28, 29].

In figure D1 we show a comparison between the analytic result and the one computed numerically by the general three-dimensional codes VMEC [53] and SIMSOPT [54]. Excellent agreement between both can be seen for both κ_1 and κ_2 .

ORCID iDs

T M Schuett © 0000-0001-5197-4348 I Cziegler © 0000-0003-1040-8918 D Dickinson © 0000-0002-0868-211X

References

- [1] Beidler C *et al* 2021 Demonstration of reduced neoclassical energy transport in wendelstein 7-x *Nature* **596** 221–6
- [2] Carralero D et al (the Wendelstein 7-X team) 2021 An experimental characterization of core turbulence regimes in wendelstein 7-x Nucl. Fusion 61 096015
- [3] Diamond P H, Itoh S-I, Itoh K and Hahm T S 2005 Zonal flows in plasma—a review *Plasma Phys. Control. Fusion* 47 R35
- [4] Fujisawa A 2008 A review of zonal flow experiments Nucl. Fusion 49 013001
- [5] Biglari H, Diamond P H and Terry P W 1990 Influence of sheared poloidal rotation on edge turbulence *Phys. Fluids B* 2 1–4
- [6] Wagner F et al 1982 Regime of improved confinement and high beta in neutral-beam-heated divertor discharges of the asdex tokamak Phys. Rev. Lett. 49 1408–12
- [7] Diamond P H and Kim Y 1991 Theory of mean poloidal flow generation by turbulence *Phys. Fluids B* 3 1626–33
- [8] Xu M et al 2012 Frequency-resolved nonlinear turbulent energy transfer into zonal flows in strongly heated l-mode plasmas in the hl-2a tokamak Phys. Rev. Lett. 108 245001
- [9] Cziegler I, Hubbard A E, Hughes J W, Terry J L and Tynan G R 2017 Turbulence nonlinearities shed light on geometric asymmetry in tokamak confinement transitions *Phys. Rev. Lett.* 118 105003, 03
- [10] Cziegler I, Tynan G, Diamond P, Hubbard A, Hughes J, Irby J and Terry J 2015 Nonlinear transfer in heated l-modes approaching the l-h transition threshold in alcator c-mod *Nucl. Fusion* 55 083007
- [11] Schmitz L 2017 The role of turbulence–flow interactions in lto h-mode transition dynamics: recent progress *Nucl. Fusion* 57 025003, 01
- [12] Dimits A M et al 2000 Comparisons and physics basis of tokamak transport models and turbulence simulations Phys. Plasmas 7 969–83
- [13] Biggs-Fox S N 2022 Spatial structure of micro-instabilities in tokamak plasmas: zonal flows and global effects in local gyrokinetic simulations *PhD Thesis* University of York
- [14] Freidberg J P 2014 Ideal MHD (Cambridge University Press)

- [15] Belli E A, Hammett G W and Dorland W 2008 Effects of plasma shaping on nonlinear gyrokinetic turbulence *Phys. Plasmas* 15 092303
- [16] Angelino P *et al* 2008 The role of plasma elongation on the linear damping of zonal flows *Phys. Plasmas* **15** 062306
- [17] Angelino P et al 2009 Role of plasma elongation on turbulent transport in magnetically confined plasmas Phys. Rev. Lett. 102 195002
- [18] Singh R and Diamond P 2022 Zonal flow screening in negative triangularity tokamaks Nucl. Fusion 62 126073
- [19] Singh R, Diamond P and Nelson A 2023 Geometric dependencies of the mean e×b shearing rate in negative triangularity tokamaks *Nucl. Fusion* 63 126053
- [20] Xu M, Tynan G R, Holland C, Yan Z, Muller S H and Yu J H 2009 Study of nonlinear spectral energy transfer in frequency domain *Phys. Plasmas* 16 042312
- [21] Camargo S J, Biskamp D and Scott B D 1995 Resistive drift-wave turbulence *Phys. Plasmas* 2 48–62
- [22] Maeyama S, Idomura Y, Watanabe T-H, Nakata M, Yagi M, Miyato N, Ishizawa A and Nunami M 2015 Cross-scale interactions between electron and ion scale turbulence in a tokamak plasma *Phys. Rev. Lett.* 114 255002
- [23] Maeyama S, Watanabe T-H, Idomura Y, Nakata M, Ishizawa A and Nunami M 2017 Cross-scale interactions between turbulence driven by electron and ion temperature gradients via sub-ion-scale structures *Nucl. Fusion* 57 066036
- [24] Holland C, Tynan G R, Fonck R J, McKee G R, Candy J and Waltz R E 2007 Zonal-flow-driven nonlinear energy transfer in experiment and simulation *Phys. Plasmas* 14 056112
- [25] Barnes M et al 2024 Gs2 v8.2.0 supported by CCP Plasma https://doi.org/10.5281/zenodo.12646925
- [26] Dorland W, Jenko F, Kotschenreuther M and Rogers B N 2000 Electron temperature gradient turbulence *Phys. Rev. Lett.* 85 5579–82
- [27] Miller R L, Chu M S, Greene J M, Lin-Liu Y R and Waltz R E 1998 Noncircular, finite aspect ratio, local equilibrium model *Phys. Plasmas* 5 973–8
- [28] Ball J, Parra F I, Barnes M, Dorland W, Hammett G W, Rodrigues P and Loureiro N F 2014 Intrinsic momentum transport in up-down asymmetric tokamaks *Plasma Phys. Control. Fusion* 56 095014
- [29] Ball J GS2 analytic geometry specification (available at: https://bitbucket.org/gyrokinetics/wikifiles/raw/master/JRB/ GS2GeoDoc.pdf) (Accessed 27 October 2023)
- [30] Frieman E A and Chen L 1982 Nonlinear gyrokinetic equations for low-frequency electromagnetic waves in general plasma equilibria *Phys. Fluids* 25 502–8
- [31] Abel I G, Plunk G G, Wang E, Barnes M, Cowley S C, Dorland W and Schekochihin A A 2013 Multiscale gyrokinetics for rotating tokamak plasmas: fluctuations, transport and energy flows *Rep. Prog. Phys.* 76 116201
- [32] Beer M A, Cowley S C and Hammett G W 1995 Field-aligned coordinates for nonlinear simulations of tokamak turbulence *Phys. Plasmas* 2 2687–700
- [33] Highcock E G 2012 The zero turbulence manifold in fusion plasmas (arXiv:1207.4419)
- [34] Frisch U 1995 *Turbulence: the legacy of A. N. Kolmogorov* (Cambridge University Press)

- [35] Ball J and Parra F I 2015 Intuition for the radial penetration of flux surface shaping in tokamaks *Plasma Phys. Control.* Fusion 57 035006
- [36] Marinoni A, Sauter O and Coda S 2021 A brief history of negative triangularity tokamak plasmas Rev. Mod. Plasma Phys. 5 6
- [37] Anand H et al 2024 Real-time plasma equilibrium reconstruction and shape control for the mast upgrade tokamak Nucl. Fusion 64 086051
- [38] Imada K et al the MAST Upgrade Team 2024 Observation of a new pedestal stability regime in mast upgrade h-mode plasmas Nucl. Fusion 64 086002
- [39] Joiner N and Dorland W 2010 Ion temperature gradient driven transport in tokamaks with square shaping *Phys. Plasmas* 17 062306
- [40] Davies R, Dickinson D and Wilson H 2022 Kinetic ballooning modes as a constraint on plasma triangularity in commercial spherical tokamaks *Plasma Phys. Control. Fusion* 64 105001
- [41] Nelson A O *et al* 2024 First access to ELM-free negative triangularity at low aspect ratio *Nucl. Fusion* **64** 124004
- [42] Parra F I, Barnes M and Peeters A G 2011 Up-down symmetry of the turbulent transport of toroidal angular momentum in tokamaks *Phys. Plasmas* **18** 062501
- [43] Ball J, Parra F I and Barnes M 2016 Poloidal tilting symmetry of high order tokamak flux surface shaping in gyrokinetics Plasma Phys. Control. Fusion 58 045023
- [44] Helander P 2014 Theory of plasma confinement in non-axisymmetric magnetic fields *Rep. Prog. Phys.* 77 087001
- [45] Xanthopoulos P, Mischchenko A, Helander P, Sugama H and Watanabe T-H 2011 Zonal flow dynamics and control of turbulent transport in stellarators *Phys. Rev. Lett.* 107 245002
- [46] Nakata M and Matsuoka S 2022 Impact of geodesic curvature on zonal flow generation in magnetically confined plasmas Plasma Fusion Res. 17 1203077
- [47] Scott B 2003 The geodesic transfer effect on zonal flows in tokamak edge turbulence *Phys. Lett. A* 320 53–62
- [48] a. Kreyszig E 1959 Differential Geometry (Mathematical Expositions) (University of Toronto Press)
- [49] Hendrik M 2024 Hendrik and on behalf of the STEP Plasma Team, Plasma burn-mind the gap *Phil. Trans. R. Soc. A* 382 20230406
- [50] Schuett T 2025 Data for the poloidal distribution of electrostatic zonal flow drive in strongly shaped tokamaks Zenodo https://doi.org/10.5281/zenodo.17431814
- [51] Told D and Jenko F 2010 Applicability of different geometry approaches to simulations of turbulence in highly sheared magnetic fields *Phys. Plasmas* 17 042302
- [52] Orszag S A 1971 On the elimination of aliasing in finite-difference schemes by filtering high-wavenumber components J. Atmos. Sci. 28 1074–1074
- [53] Hirshman S P and Whitson J C 1983 Steepest-descent moment method for three-dimensional magnetohydrodynamic equilibria *Phys. Fluids* 26 3553–68
- [54] Landreman M, Medasani B, Wechsung F, Giuliani A, Jorge R and Zhu C 2021 Simsopt: a flexible framework for stellarator optimization J. Open Source Softw. 6 3525